NUMERICAL AND EXPERIMENTAL INVESTIGATION OF COMPOSITE HEAT PIPE TECHNOLOGY

BY

KEITH COULSON

THESIS

Submitted in partial fulfillment of the requirements
for the degree of Master of Science in Mechanical Engineering
in the Graduate College of the
University of Illinois at Urbana-Champaign, 2018

Urbana, Illinois

Advisors:

Associate Professor Sanjiv Sinha
Assistant Professor Nenad Miljkovic

ABSTRACT

Heat pipes are heat transport devices that pose very small thermal resistance to heat flow, even over relatively long transport paths. Utilizing two-phase heat transfer, they can transport heat from confined spaces to remote heat sinks where more surface area might be readily available. This attribute is particularly useful in multiple thermal management applications, such as power generation, electronics cooling, and permafrost retention. To improve specific (per unit mass) performance and reduce manufacturing cost, we present here a concept for a composite heat pipe that utilizes different materials for the adiabatic and evaporator/condenser sections. Such composite heat pipes can be fabricated with low cost materials, while maximizing specific heat transfer performance. We present a mathematical model of heat transport in the composite heat pipe that accounts for the pressure driven flow of the vaporized working fluid, the pressure drop over the length of the wick, and the thermal resistances governed by the wall, wick, liquid, and vapor. We use the model to show that the composite heat pipe has the potential for identical effective thermal conductivity when compared to its all metal counterpart, with drastic improvement (1000%) in specific performance. We further use the model to perform sensitivity analysis and parametric multi-objective design optimization with respect to specific performance maximization and cost minimization. Finally, we design and build an apparatus to experimentally test

how substituting the adiabatic section metal wall with a non-metal material impacts heat pipe performance. Our work offers a design platform for the development of next generation thermal transport devices that reduce cost and weight, and maximize manufacturability. They facilitate implementation flexibility through modular design and integration schemes conducive to additive manufacturing techniques.

To Victoria, for all her love and support

ACKNOWLEDGMENTS

I gratefully acknowledge all the time and effort spent on my behalf by Dr. Sanjiv Sinha and Dr. Nenad Miljkovic. Their guidance was integral to the completion of this work. It was with their constructive criticism, encouragement, and direction with which this degree was earned. With them I have grown both as a researcher and as a person, and I am thankful that they were a part of my education. I also want to thank the many collaborators who provided assistance through their experience and actions. Special thanks to Druv Gelda, Manju Chinnappamudaliar Rajagopal, Emil Annevelink, Josh Schiller, Tom Foulkes, Junho Oh, Krishna Valavala, Daniel Hsieng, Seyi Babatola, and the rest of the Sinha and Miljkovic research groups.

TABLE OF CONTENTS

CHAPTER 1

INTRODUCTION

1.1 Background and Motivation

Heat pipes can transport heat over long distances without introducing significant additional thermal resistance. The effective thermal conductivity of heat pipes can be several orders of magnitude larger (∼10 kW/mK) than the bulk material of which they are made (∼100 W/mK). Heat pipes are employed in thermal applications, ranging in size and scale from desktop and laptop systems [1], satellites [1], video game consoles [2], HVAC&R technology [2], Alaskan permafrost preservation [3], and many others. Figure 2.1a shows the typical structure of a heat pipe that comprises a hermetically sealed metal container with an internal wick structure and a working fluid at a prescribed saturation pressure inside [1]. Different metals, wicks, and working fluids can be selected depending on the specific operating environment. The functioning of heat pipes is well studied. A heat pipe can be divided into the evaporator, adiabatic, and condenser sections. Heat applied to the evaporator section conducts through the container wall and vaporizes the working fluid, building vapor pressure inside the core of the evaporator section. The elevated pressure drives the vapor through the adiabatic section to the condenser, which is at a lower temperature than the evaporator. Latent heat from the condensed vapor is conducted across the wall to a heat sink. The

capillary pressure of the working fluid pumps it back to the evaporator section through the wick structure.

1.2 Modular Composite Heat Pipes

An important aspect of heat transfer in heat pipes is that conduction heat transfer through the axial length of the heat pipe wall and wick is negligible compared to the highly effective heat transfer via the vapor core. Conduction through the wall matters mainly at the evaporator and condenser sections. Here, we investigate the idea of using lightweight and/or cheaper materials for the adiabatic section that typically possess low thermal conductivity. We show that a heat pipe with a non-metal adiabatic section can possess higher specific thermal conductivity than an all-metal heat pipe using the same parameters. Such modular composite heat pipes (MCHP) can be attractive for applications in mobile environments where reduced weight is desirable. For example, thermal management systems in satellites can be made lighter, allowing for more weight for other parts of the system.

In this work, we develop a fast and efficient 1-D heat pipe model. Using that model, we perform optimization, sensitivity, and case study analysis, and design and build an experimental apparatus to verify the simulations. The model incorporates heat and mass transfer through porous media, liquid-vapor interfacial heat transfer, and axial heat conduction, among other processes. Given a specific heat input, we calculate wall and working fluid temperatures, which are used to determine limits for the heat pipe performance. Using this information, we show that adiabatic section wall material does not impact heat pipe limits, and in fact substituting metal for a non-metal in this area can greatly improve specific

performance.

We then utilize the model in a variety of optimization and sensitivity analyses. We perform a geometric sensitivity study, where we show that the heat pipe power limits are not sensitive to changing adiabatic section material. We then perform a parametric study by changing adiabatic material and geometry of the heat pipe. This shows that heat pipes with adiabatic sections made from ABS instead of copper exhibit better specific effective thermal conductivities ($k_{eff}{}'$). Finally we use Monte Carlo analysis to find combinations of geometry and adiabatic section material optimized to cost, specific performance, and $k_{eff}{}'$. These results are used to calculate bulk material cost savings potential in CPU cooling and permafrost retention applications.

A thermal test apparatus was designed and built to test heat pipes, both homogeneous and modular. The heat input is determined through direct calorimetry instead of heater power, which should improve the accuracy of the experimental results. The fabrication procedure and experiment construction are discussed, along with preliminary results and future work.

Finally, we highlight some challenges to MCHP development, as well as experimental design improvements.

1.3 Structure of the Thesis

The rest of the thesis is organized as follows.

In Chapter 2, we develop a one-dimensional model to determine performance results of cylindrical heat pipes. These performance results include maximum heat input before dryout, wall and fluid temperatures, and vapor pressures.

In Chapter 3, we use the model developed in Chapter 2 to perform sensitivity and optimization analyses for different adiabatic wall materials. Both cost and specific performance are optimized, as well as the sensitivity that altering geometric conditions have on the maximum allowable heat input.

Chapter 4 outlines and examines the fabrication and thermal test design. Error sources and analysis are also discussed.

Finally, we summarize the findings in Chapter 5. Future experimental work and barriers to success will also be discussed.

CHAPTER 2

1-D HEAT PIPE PERFORMANCE MODEL

Here, we develop a one-dimensional heat transfer model for MCHPs to mainly investigate their specific thermal conductivities and maximum heat inputs. The performance of MCHPs is compared against conventional heat pipes in specific applications such as consumer-grade electronics and permafrost retention. We further use the model to investigate sensitivity to geometric parameters and perform a multi-objective optimization to identify optimal values for these parameters. The results show that plastics such as ABS and PVC offer the best specific performance and are attractive candidates for the fabrication and implementation of MCHPs. This study provides a framework for the future design, fabrication, and implementation of MCHPs with the objective of minimizing weight and materials cost while maximizing performance.

The governing transport processes in a heat pipe (Figure 2.1a) can be generalized into three categories: (1) flow of vapor in the core, (2) heat conduction through the pipe wall, and (3) liquid flow through porous media [5]. A thermal resistance network can be used to model these processes [5]. Figure 2.1b and Table 2.1 show thermal resistance network for a heat pipe along with representative values for various resistances [4]. To calculate the temperature drops via conduction through the wall and wick, thermal resistances were calculated using the properties of the heat pipe materials. For the vapor core, the Clausius-

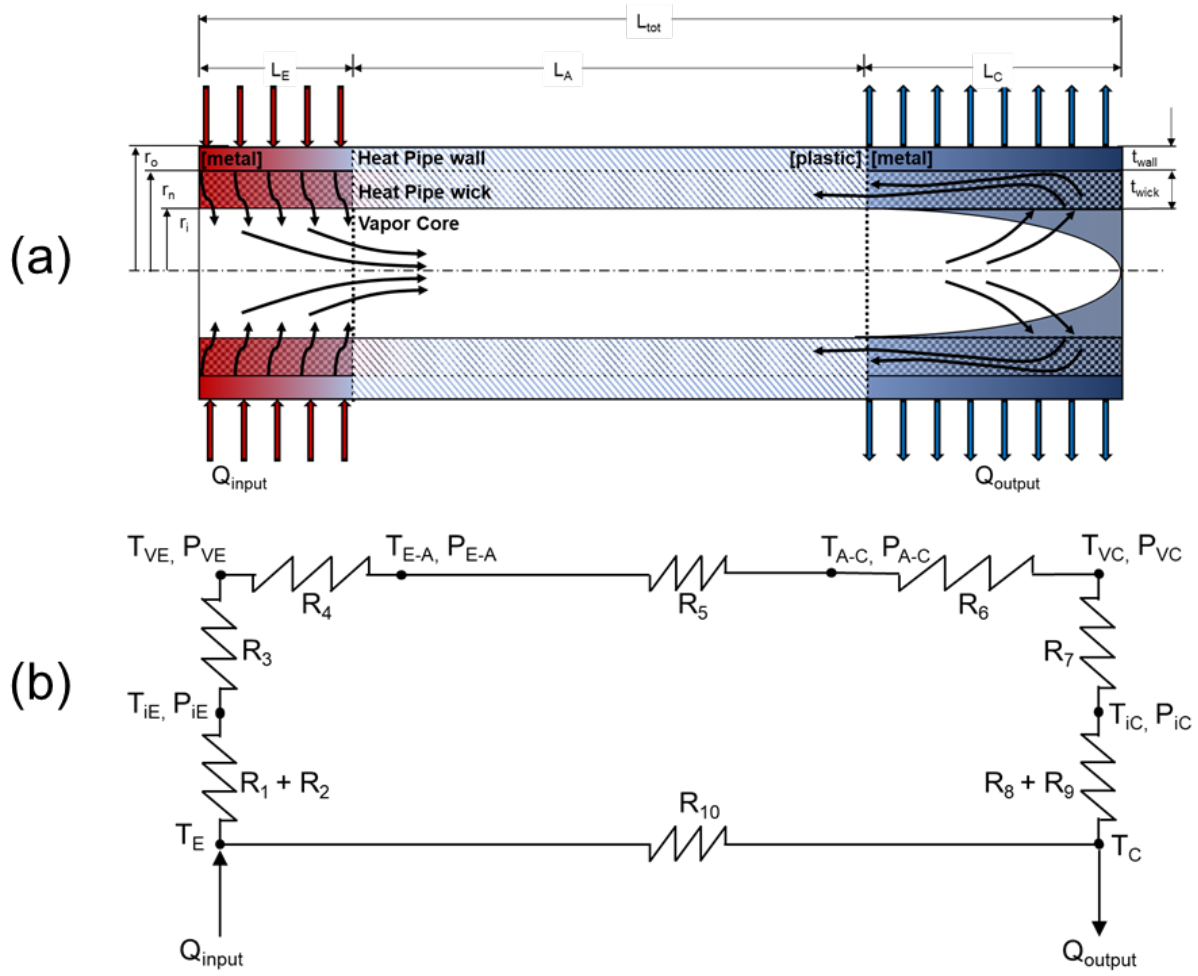

Figure 2.1: (a) Schematic of a standard constant conductance heat pipe showing the heat transport operation and circulation of the working fluid (b) Thermal resistance model of constant conductance heat pipe operation used to simulate temperatures within the device given specific heat inputs

Table 2.1: Representative orders of magnitude for heat pipe thermal resistance network [4].

Resistance	Description	Characteristic Value [K cm^2/W]
R_1	Wall radial resistance - evaporator	10^{-1}
R_2	Wick radial resistance - evaporator	10
R_3	Liquid-vapor interface - evaporator	10^{-5}
R_4	Vapor pseudo resistance, evaporator to adiabatic	10^{-8}
R_5	Vapor pseudo resistance, adiabatic	10^{-8}
R_6	Vapor pseudo resistance, adiabatic to condenser	10^{-8}
R_7	Wall radial resistance - evaporator	10^{-5}
R_8	Wick radial resistance - condenser	10
R_9	Wall radial resistance - condenser	10^{-1}
R_{10}	Wall + wick axial resistance	10 - 10^3

Clapeyron equation [4] the relationships between the pressure and temperature at saturation was used to calculate the changes of each property. Specifically, resistances R_4, R_5, and R_6 obey

$$\frac{dP_V}{dT_V} = \frac{h_{fg} P_V}{\mathbf{R} {T_V}^2} \tag{2.1}$$

where P_V and T_V are the working fluid saturation pressure and temperature, respectively, h_{fg} is the latent heat of phase change, and $\mathbf{R}$ is the working fluid gas constant. In the vapor core the temperature difference is dependent on the pressure difference. Therefore, to relate the temperature changes from nodes 4, 5, and 6, the corresponding pressure changes between the nodes must be calculated. Individual sections of the heat pipe experience different vapor pressure differences within their respective cores. For this model, a 1-D approximation was used that does not assume full pressure recovery [4]. The evaporator section experiences vapor pressure buildup from the vaporization of the liquid in the wick, which can be modeled as suction from the wick such that:

$$P_{E-A} - P_{VE} = \frac{\dot{m}^2}{8\rho_V {r_i}^4} \tag{2.2}$$

where P_{E-A} is the pressure difference between the evaporator vapor core (node E) and the start of the adiabatic section, P_{VE} is the pressure difference between the liquid-vapor interface (node V) and E, $\dot{m}$ is the vapor mass flow rate through the core, ρ_V is the vapor density, and r_i is the internal radius of the circular heat pipe. The condenser section experiences a similar but reversed vapor pressure drop [4]:

$$P_{VC} - P_{A-C} = -\frac{4}{\pi^2}\frac{\dot{m}^2}{8\rho_V {r_i}^4} \tag{2.3}$$

where P_{VC} is the pressure difference between node V and the condenser vapor core (node C) and P_{A-C} is the pressure difference between the end of the adiabatic section and node C.

The adiabatic section does not introduce or remove heat, and only acts as a transport section. In this region, the vapor is assumed to be fully developed laminar pipe flow with pressure drop:

$$P_{A-C} - P_{E-A} = \frac{8\mu_V \dot{m}}{\rho_V \pi {r_i}^4} L_A \tag{2.4}$$

where μ_V is the vapor viscosity and L_A is the length of the adiabatic section (Figure 2.1a).

The wick and wall both can be generalized as concentric cylinders, however while the container wall is a solid material with an isotropic thermal conductivity, the effective thermal conductivity of the wick is different for the evaporator and condenser sections. The radial thermal resistances of the wall at the evaporator (R_1) and condenser sections (R_9) were

calculated as [6]:

$$R_1 = \frac{\log(\frac{r_o}{r_n})}{2\pi L_E k_S} \tag{2.5}$$

$$R_1 = \frac{\log(\frac{r_o}{r_n})}{2\pi L_C k_S} \tag{2.6}$$

where r_n is the wall inner radius, L_E is the evaporator length, L_C is the condenser length (Figure 2.1a), and k_S is the wall material thermal conductivity.

2.1 Wick Flow and Heat Transfer

The selection of a wick structure is of paramount importance for the effective operation of a heat pipe [2]. Based on previous studies and characterizations [7], a grooved wick design was utilized in our model due to its high-performance limits and manufacturability. The width of the fins and the groove channels were selected based on the radius of the pipe. The meniscus of the fluid within the channels provides the curvature used for the capillary pressure drop calculations for the fluid inside the wick. Since all channels are identical in the model, that capillary pressure drop was the same in every channel and not a function of the radial position. The fluid flow in the channel was modeled under the assumptions that: (1) the channels are uniform, isotropic, and that there is enough liquid to fully charge the wick, (2) the liquid properties are determined by the average temperature of the liquid in the wick, and (3) the pressure drop along the length of the wick (axial) is uniform. Furthermore, the channels are assumed to be perfectly wetting, providing the largest possible interface curvature and capillary pressure budget.

To calculate the thermal conductivity of the wick, the liquid void fraction (ε) was calculated as a function of the channel width (w_g) and the fin thickness (w_f):

$$\varepsilon = \frac{w_g}{w_g + w_f} \tag{2.7}$$

Using the liquid void fraction, the thermal conductivity of the wick was calculated assuming heat flows in a parallel manner. The assumption is appropriate given the parallel groove structure of the wick. The wick thermal resistance at the evaporator (R_2) and condenser (R_8) sections differs. At the evaporator, the most of the heat is transported via evaporation from the liquid at the base of the grooves, whereas in the condenser section, the grooves are flooded, and the fins and the liquid remove heat in a parallel fashion. To account for this, the resistance in the evaporator is a function only of the liquid thermal conductivity, neglecting the fins, whereas the condenser uses the wick effective thermal conductivity. The wick thermal conductivity was calculated using [4]:

$$k_w = k_S(1 - \varepsilon(1 - \frac{k_L}{k_S})) \tag{2.8}$$

with corresponding resistances of [4]:

$$R_2 = \frac{1 - \frac{\pi}{4}}{2k_L L_E N} \tag{2.9}$$

$$R_8 = \frac{\log(\frac{r_n}{r_i})}{2\pi L_C k_w} \tag{2.10}$$

2.2 Liquid-vapor interface

To accurately model the interfacial mass transfer during phase change at the liquid-vapor interface, we assumed the heat pipe is filled with a pure saturated vapor and that the presence of impurities and non-condensable gases is negligible. Hence, the interfacial heat transfer coefficient can be modeled as [8]:

$$h_i = \frac{2\alpha}{(2-\alpha)\sqrt{2\pi RT}} \frac{{h_{fg}}^2}{v_g T} \tag{2.11}$$

where $\alpha = 0.5$ was assumed for the evaporation and condensation coefficient [8]. Although more accurate interfacial heat transfer coefficient formulations derived from kinetic theory are available [9–12], they have not been used here due to difficulty of implementation into an analytical based heat transfer model. The interfacial heat transfer coefficient was used to calculate the thermal resistance exhibited by the liquid-vapor interface as in the evaporator (R_3) and condenser (R_7) sections as:

$$R_3 = \frac{1}{h_i 2\pi r L_E} \tag{2.12}$$

$$R_5 = \frac{1}{h_i 2\pi r L_C} \tag{2.13}$$

Changing α from 0.1 to 0.9 produces a range of interfacial resistances from $\sim 3\times10^{-7}$ to $\sim 2\times10^{-8}$ K/W. The temperature profile is not significantly affected by this change, as the interfacial heat transfer coefficient is inherently high. We note that here we assume the void fraction of the grooves to be high and do not consider it in the interfacial heat transfer resistance calculations. This assumption is appropriate due to the low characteristic thermal

resistance of the liquid-vapor interface compared to the remaining resistances in the system.

2.3 Solution Algorithm

The analytical model was solved numerically in the horizontal configuration to eliminate gravitational effects, with a fixed condenser wall temperature T_C, and input heat flux q_{in}''. Assuming that no heat loss within the system, the temperatures and pressures were calculated at each node, starting at the condenser outer wall (T_C) and working back to the evaporator outer wall (T_E). To achieve a solution, the pressure and temperature differences between each node were calculated as well. For the first iteration, we assumed that no heat is transported axially through the wall and wick by conduction. Once the evaporator outer wall temperature was calculated, the effective resistance of the heat pipe was determined. The calculated effective resistance, and the conductive resistance of the heat pipe container, R_{10}, were accounted for, and all temperatures and pressures recalculated. The convergence criterion of the model was the sum of the node temperature difference between iterations must be less than 1 x 10^{-12}. Based on the model, it was found that approximately 0.01% of the heat was transported axially through the wall from evaporator to condenser. After each heat flux input calculation, the fundamental heat pipe limits were checked for each iteration. If no limits were reached, the heat flux was increased by a predetermined increment (0.01 W/cm^2), and the model reset and solved again until convergence was reached.

The fundamental limits considered in our model were the pressure [5], sonic [13], and physical limits (i.e. heat fluxes greater than 1 kW/cm^2 and total heat inputs exceeding 3 kW). For proper operation, the wick in the evaporator section must be fully charged. This

means that the capillary pressure driving liquid flow from condenser to evaporator (ΔP_{cap}) can overcome the adverse pressure applied by a combination of vapor pressure (ΔP_V), and the viscous pressure drop inside the wick (ΔP_L) (i.e. $\Delta P_{cap} \leq \Delta P_L + \Delta P_V$). If the capillary pressure is overcome, the liquid no longer fills the wick in the evaporator, and the heat pipe ceases correct operation. The capillary pressure is a function of the channel radius and was calculated as:

$$\Delta P_{cap} = \frac{4\sigma}{w_g} \tag{2.14}$$

where σ is the liquid surface tension. The viscous liquid pressure drop inside the grooved wick was calculated using:

$$\Delta P_L = \frac{8\mu_L L_{tot}\dot{m}}{\pi\rho_L N {r_i}^4} \tag{2.15}$$

The vapor pressure drop inside the heat pipe core was taken as the sum of the pressure drops along the length of the heat pipe (sum of Equations 2.2, 2.3, 2.4, and 2.15). Within the core of the heat pipe, the vapor was assumed to be laminar and incompressible. Once the vapor velocity exceeded 0.3 times the speed of sound, incompressibility no longer held, and the heat transfer behavior can no longer be characterized by this model [4, 13].

The model was verified by comparing the temperature profile output by the model to experimental results from an all-metal heat pipe with a single heat source [14]. The model wall temperatures were $\leq 0.3\%$ different than the reported temperatures.

CHAPTER 3

MODEL RESULTS AND ANALYSES

Using this model, multiple analyses were performed based on parametric geometry and material alterations. The speed of the model allowed for large-scale optimization analyses as well. The following sections detail the results of this work, which can be used to govern future experimental directions.

3.1 Geometric Sensitivity

Prior to optimization and analysis of the model results, the sensitivity of the heat pipe geometry was investigated on the input heat flux (${q_{in}}''$). Each geometric variable (r_o, t_{wall}, t_{wick}, L_E, L_A, and L_C) was individually increased, and the maximum allowable heat input was calculated. The sensitivity curves ($\partial \ln({q_{in}}'')/\partial \ln(x)$) for each variable x were computed. The non-dimensional curves describe the effect of changing each component on the maximum heat input. Negative values indicate that increasing the variable leads to a decrease in the heat input.

Figure 3.1 shows the sensitivity to the maximum allowable heat input to the MCHP with respect to geometric parameter length scale. The parameters showing highest sensitivity were the outer radius, wick thickness, wall thickness, and adiabatic section length. Intuitively, these parameters have significant influence on heat transfer performance and represent sig-

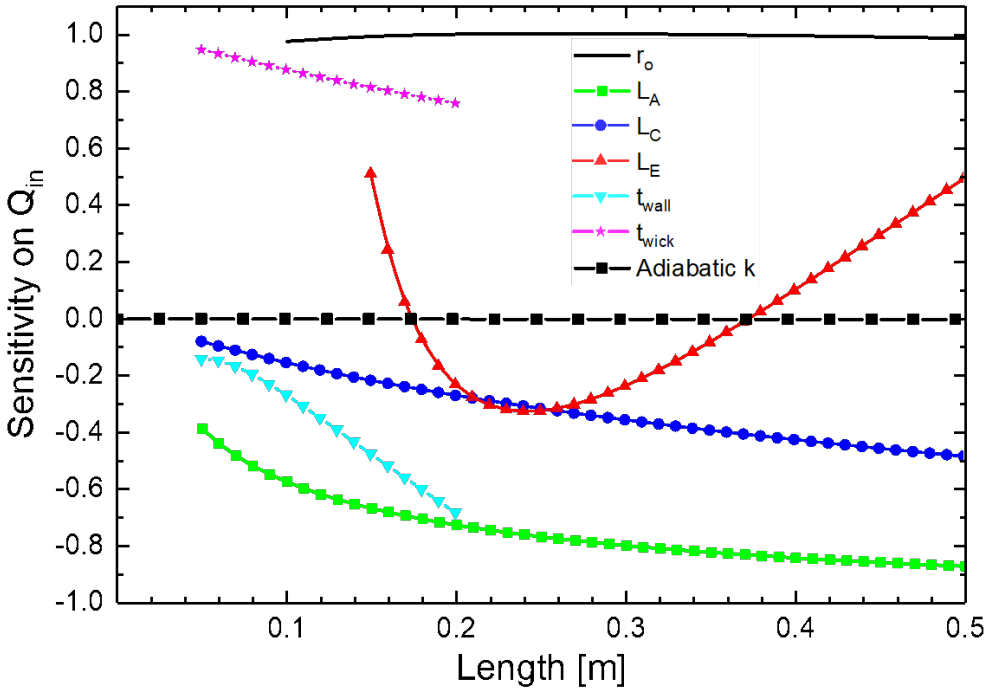

Figure 3.1: Sensitivity analysis results from simulations where each component was systematically changed while keeping other components constant. The x-axis describes the length values for each component, where the lengths of the evaporator, condenser, and adiabatic sections are shown, r_o is increased from 2 mm to 10 mm, and the thicknesses of the wall (t_{wall}) and wick (t_{wick}) are increased from 0.5 mm to 2 mm. The y-axis describes the order of magnitude effect that changing each component has on the maximum allowable heat input. For example, at small lengths increasing the evaporator has a lessening effect on the maximum heat input; however, after a certain length the effect on the heat input becomes more pronounced. Increasing the radius has a constant effect on the maximum allowable heat input.

nificant thermal resistances in the system, i.e. wall and wick thickness have the highest order of magnitude resistances outlined in Table 2.1, hence their sensitivity on maximum heat flux. Furthermore, the adiabatic section length has significant effect on the viscous pressure drop inside the wick (Eq. 2.15); hence, it represents a limitation to the capillary pumping mechanism and maximum heat transfer in the device. To better understand the validity of our proposed MCHP device, Figure 3.1 shows that the adiabatic section thermal conductivity has no effect on the maximum device heat flux, verifying the concept from a theoretical standpoint.

The results of the sensitivity analysis help to identify MHCP parameters that dominate heat transfer performance. We first used the model to understand how the geometry affects specific performance. We systematically increased the evaporator, condenser, and adiabatic lengths, along with the outer radius, and calculated the maximum heat inputs for the devices. Using the that heat input value, the geometry and weight of the device, and the temperature drop between T_E and T_C, we defined a specific effective thermal conductivity as:

$$k_{eff}{}' = \frac{(L_E + L_C + L_A)}{m_{total}} \frac{Q}{T_E - T_C} \tag{3.1}$$

where m_{total} is the mass of the device, and Q is the heat input to the device. Heat pipes are generally characterized by an effective thermal conductivity (k_{eff}) that does not account for mass. However, $k_{eff}{}'$ was chosen as an ideal metric as it rewards higher thermal performance (thermal conductivity) and penalizes higher mass (material density) for a specific heat pipe geometry. Each length was tested individually for outer radii ranging from 5 to 10 mm in increments of 1 mm. For each radius, lengths of the evaporator, condenser, and adiabatic

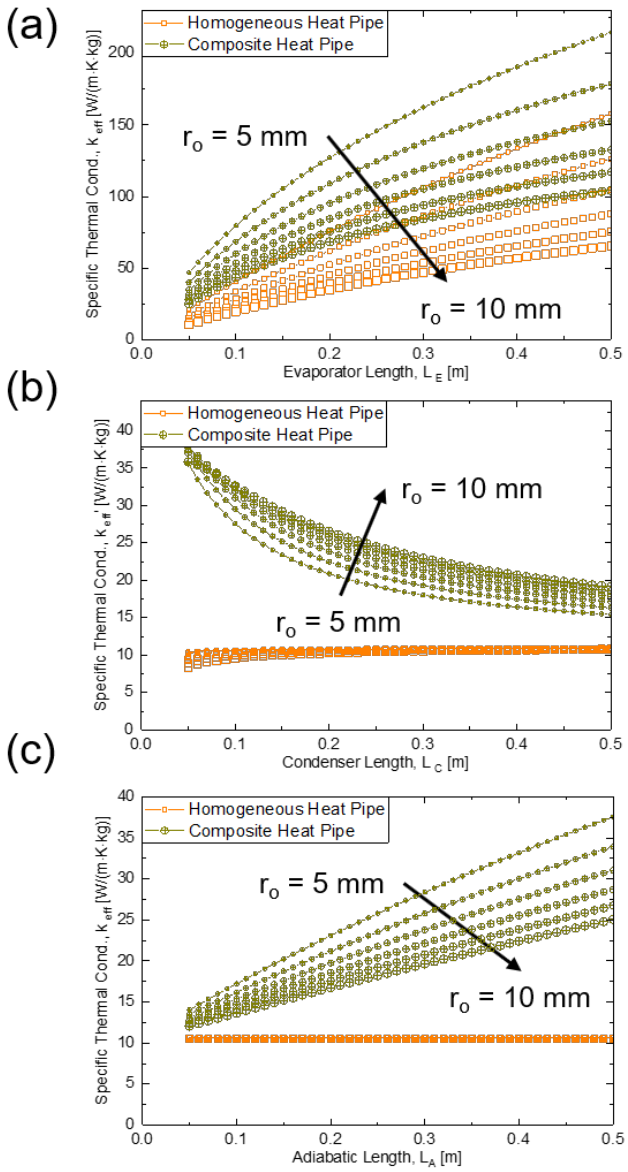

Figure 3.2: Analysis results from simulations where the evaporator length (a), condenser length (b), and adiabatic length (c), and outer radius were systematically changed while keeping other component ratios constant

section were varied individually, with other lengths and thicknesses defined as ratios of the outer radius [14]. Furthermore, copper heat pipes and MCHPs with ABS adiabatic sections were tested. In each case, increasing the outer radius of the heat pipe negatively affected $k_{eff}{}'$ due to the increased overall mass of the device (Figure 3.2a). Although greater radii allow for a corresponding increase in maximum heat input, the effect of increased mass outweighed the benefit of higher heat flux. It should be noted that lengthening the evaporator increased the maximum allowable heat input, hence increasing $k_{eff}{}'$. Furthermore, heat pipes with ABS adiabatic sections were lighter and exhibited identical heat transfer performance, resulting in higher $k_{eff}{}'$ values. Similar trends can be seen for varying the condenser length (Figure 3.2b). However, for the MCHP results, an opposite trend was observed due to the higher mass of the condenser and negligible increase in overall heat transfer performance with higher condenser length. The trend is reversed in this case because the increased mass dominates the increased performance of a heat pipe with a longer condenser section. The reverse trend can be further explained by noting that the evaporator is nominally 25% the length of the condenser.

Figure 3.2c shows $k_{eff}{}'$ as a function of composite adiabatic section length. While lengthening the adiabatic section reduces the maximum allowable heat input to the device (4 W/cm^2) due to larger viscous pressure drop, it also drastically increases $k_{eff}{}'$. In all-copper heat pipes, $k_{eff}{}'$ remains unchanged due to the viscous pressure drop balancing with the longer heat conductance. Lengthening of the ABS adiabatic section improved $k_{eff}{}'$ by $\sim$350% when compared to the all-copper heat pipe. This is due to the reduced density of the adiabatic section material.

3.2 Optimization

The above model can predict the performance of heat pipe geometries based on fixed parameters that are known. However, due to the large parametric design space coupled with the lack of non-dimensional groups to characterize the system, we employed a multi-objective optimization to identify the peak performance of MCHPs. Specifically, the three main objectives to be optimized were $k_{eff}{}'$, specific performance (β), and the bulk cost of the device (Γ).

Table 3.1: Material properties used in the multi-objective optimization analysis.

Material	Density [kg/m^3]	Thermal Conductivity [W/mK]	Bulk material cost [USD/kg]	Raw mat. H_2O compatibility	CTE 10^{-6} [m/mK]	Outgassing [%TML] [15]	Elastic Modulus [GPa]
SS	7700	16	2.70	Yes	17.3	0.00	180
Ni	8900	91	6.10	Yes	13.0	0.02	170
ABS	721	0.18	0.72	No	72-108	0.94	1.4-3.1
Cu	8960	397	7.08	Yes	16-16.7	0.00	117
PP	900	0.20	0.60	No	72-90	2.82	1.5-2
PVC	833	0.19	0.45	No	54-110	30.67	2.4-4.1
HDPE	1000	0.48	0.61	No	108	0.58	0.8
Rubber	801	0.10	1.59	No	80	5.01	0.01-0.1
PET	1380	0.20	0.37	No	59.4	0.61	2-2.7
PMMA	1190	0.21	3.00	No	70-77	0.68	2.4-3.4
Glass	2600	1.05	1.35	Yes	5.9-9.0	0.74	50-90
Iron	7870	80	0.20	Yes	12.0	0.00	210
Al	2700	205	1.80	Yes	21-24	0.05	69

To study a wide spectrum of potential materials, 13 different materials having differing thermophysical properties (Table 3.1) were tested as adiabatic sections. The multi-objective optimization was conducted by computing the performance of each individual material with 10,000 different combinations of evaporator, adiabatic, and condenser lengths, as well as outer radii. The wick and wall thicknesses were kept constant at 0.1 mm and 1 mm, respectively. The outer radii, evaporator lengths, and adiabatic and condenser lengths for each

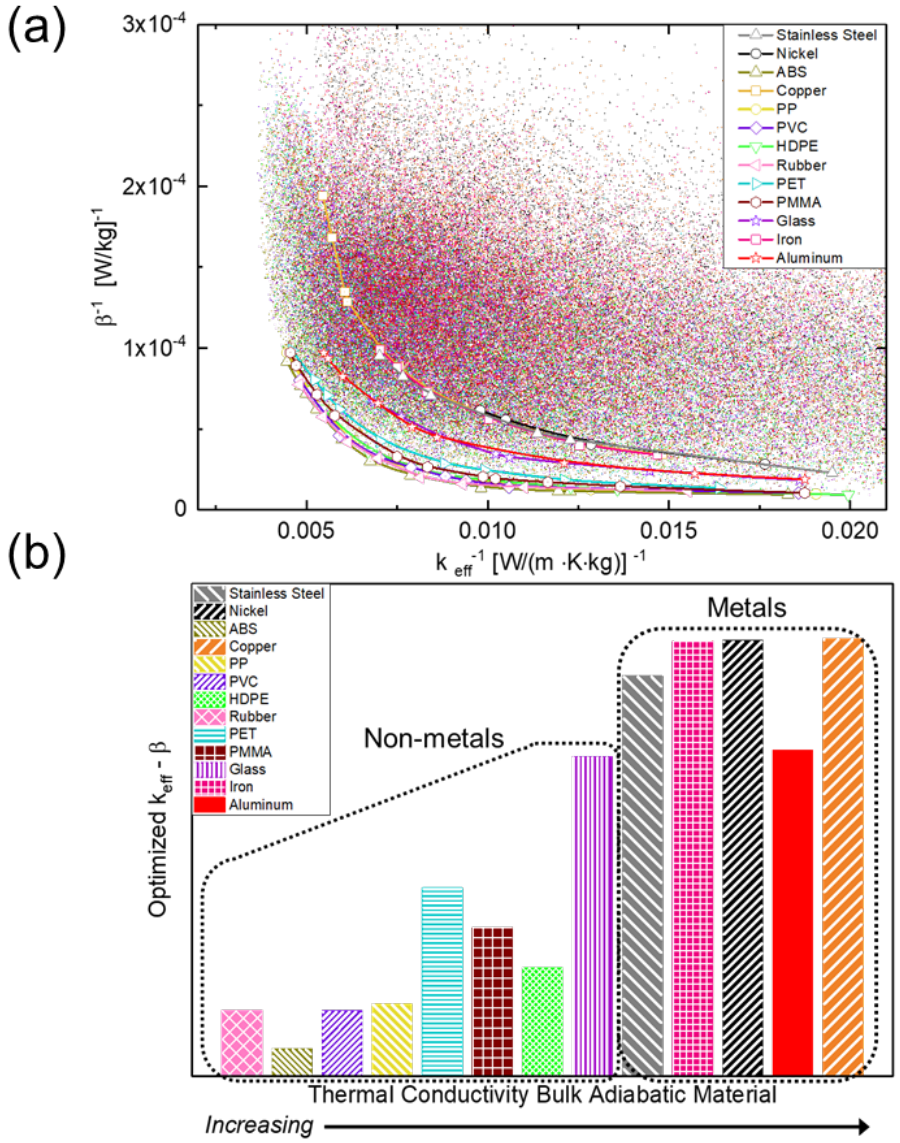

Figure 3.3: (a) Monte Carlo analysis results for 13 different adiabatic section materials, comparing the devices specific thermal conductivity and the device weight per Watt of heat transported, with the fronts for each material highlighted, and (b) the optimal value for each front in the order of the material bulk thermal conductivity.

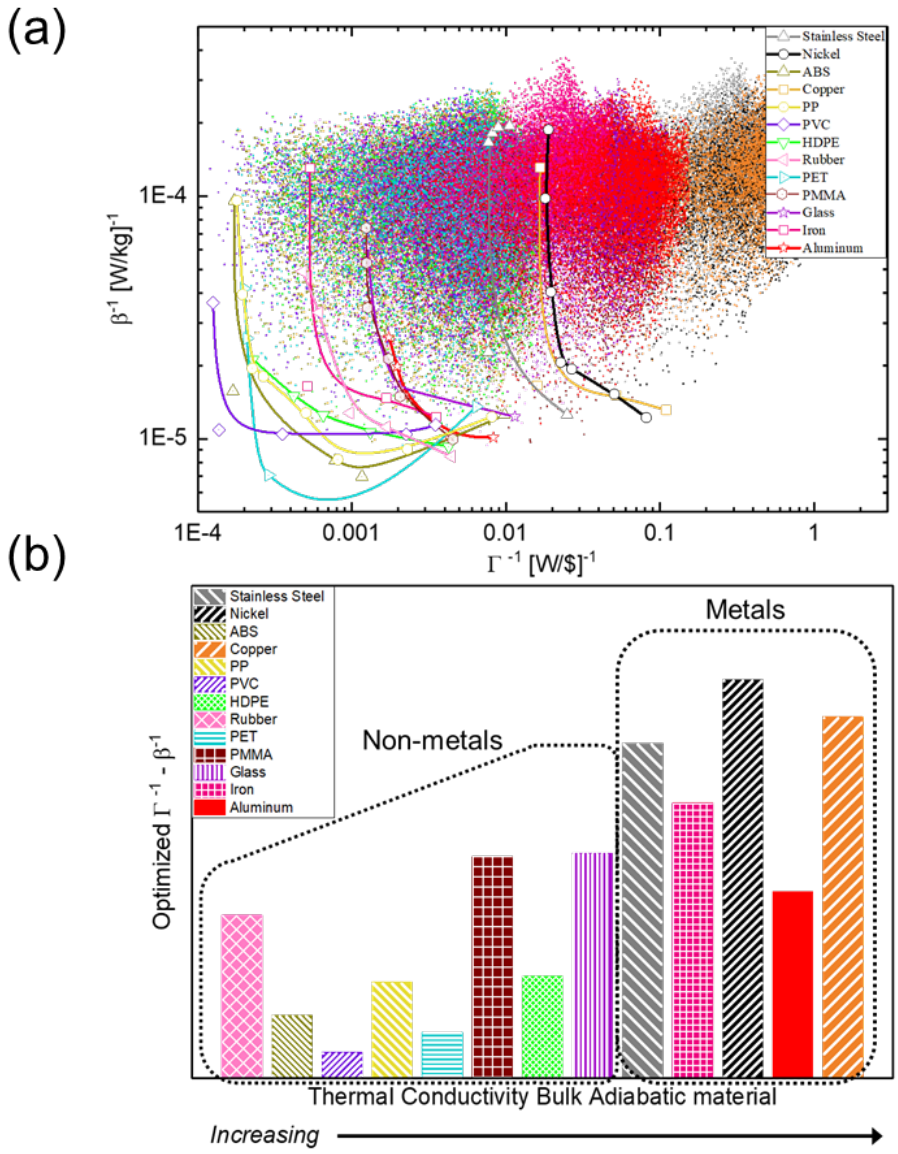

Figure 3.4: Monte Carlo analysis results for 13 different adiabatic section materials, comparing the cost and device weight per Watt of heat transported, with the fronts for each material highlighted, and (b) the optimal value for each front in the order of the material bulk thermal conductivity

device tested ranged from 5 to 10 mm, 50 to 500 mm, and 10 to 500 mm, respectively.

Figure 3.3a shows the multi-objective optimization of the inverse of specific performance (β^{-1}) as a function of the inverse of specific thermal conductivity (${k_{eff}}'^{-1}$). The optimization results were plotted in this manner to ensure that each independent axis represented the best design when the design point was closest to the origin (0, 0). The results show that the most efficient MCHP designs have plastic adiabatic sections. To better quantify the results, the Pareto frontier was computed for each material optimization, and plotted in Figure 3.3b. Each Pareto front represents the geometries for each material that provide combinations of the largest ${k_{eff}}'$ and β. Due to the insensitivity on heat transfer performance of the adiabatic section material, the multi-objective optimization results indicated decreasing optimal performance as a function of higher material density. To identify the optimum design from the front, the product of the two objective parameters (${k_{eff}}'^{-1} \times \beta^{-1}$) was computed and the minimum value reported. As expected, plastics showed the most optimum designs.

Although total mass of the MCHP design coupled with thermal performance represent one pair of optimization parameters, material cost is a big factor when considering the implementation of heat pipe technologies [16]. As a secondary multi-objective optimization, we considered the bulk cost of the device based simply on the volume of copper and adiabatic material needed to achieve the design. Manufacturing costs and implementation considerations with respect to dissimilar materials were not considered in this analysis. Figure 3.4a shows β^{-1} as a function of the inverse cost effectiveness of the device (Γ^{-1}). As in Figure 3.3b, the results showed local clustering based on material type (i.e. plastic, metal, ceramic, semiconductor, etc.) as identified by the dotted regions. To better understand the optimum

design for each material type, the Pareto frontier was computed and plotted in Figure 3.4a. Although iron was found to be the least expensive material per kilogram ($\sim$0.20/kg, pricing on 2/19/2018), the high density of iron (7870 kg/m^3) resulted in non-optimal overall performance. Furthermore, the material thermal conductivity did not exhibit any direct influence on the performance of the MCHPs, providing further verification that the MCHP concept is an ideal alternative to an all-metal heat pipe. Figure 3.4b plots the optimum Pareto frontier design point as a function of the material thermal conductivity for the two objective parameters considered ($\beta^{-1} \times \Gamma^{-1}$). Similar to the results considering mass, the plastics showed the most optimum designs.

3.3 Benchmark Test Cases

Although the previous model development, sensitivity analysis, and multi-objective optimization clearly show potential for MCHPs, a better understanding of how MCHPs can affect real life applications is required. To facilitate a clear comparison with state of the art (SOA) heat pipe designs, two test cases were selected to represent small and large-scale applications. Large scale heat pipes, such as those used on oil pipeline struts in Canada and Alaska [3, 17], are used to ensure that the permafrost that the support structures are built on do not lose the rigidity that the permafrost provides. Constant conductance heat pipes (CCHPs) are placed with the evaporator sections in the ground and the condensers exposed to the outside environment. They operate by removing heat from the ground and releasing it to the colder outside air, maintaining the permafrost and structural integrity of the supports. One difficulty with modeling heat pipes for permafrost retention was design-

ing the correct length of the MCHP [17]. Depending on the depth, heat pipes can range in length from 9 to 25 m long. Using MCHPs, evaporator lengths could be standardized, and length adjustments made with PVC adiabatic sections. PVC is readily available in the dimensions needed and has a bulk material cost 54% that of the steel used for current SOA permafrost heat pipes. The dimensions used for permafrost heat pipe comparison included averaged evaporator and condenser lengths, with 2-inch outer diameters and 0.5-inch wall thicknesses.

In consumer electronics computer systems, heat pipes are commonly used to transport heat from processors to fin-fan heat sinks [5]. For desktop computers, custom or off-the-shelf heat sinks often incorporate multiple heat pipes for even more efficient heat transport [4]. In laptops, the customer does not generally change these devices, and single, flat CCHP's are used to transport the heat to the heat sink, since space is at a premium. The transport distance from the heat generating device and the heat sink in commercial laptops generally does not exceed 10 cm. [1]. With that in mind, the test cases were limited to $L_E < 1$ cm, $L_C < 5$ cm, and 1 cm $< L_A <$ 10 cm, with 2 mm $< r <$ 20 mm. Here, we modeled sintered and wrapped-screen wicks as opposed to the earlier grooved wicks. However, the two wick designs showed negligible difference, with heat fluxes on the same order of magnitude.

The two test cases were run to compare the performance characteristics, cost, mass, and multi-objective parameters with the SOA all metal heat pipes. For permafrost applications, the cost and mass reduced by 50% and 48%, respectively, with a corresponding maintenance of performance when compared to the SOA design. Similarly, for the electronics cooling applications, the cost and mass reduced by 69% and 55%, respectively, with similar perfor-

mance to SOA. The benchmark comparisons showed in Table 3.2 demonstrate the utility of MCHPs as future thermal management devices that can significantly enhance SOA designs in terms of mass, cost, and flexibility, while maintaining identical performance.

Table 3.2: Comparison of state-of-the-art and composite heat pipe performances, weights, and bulk material costs for 100,000 units at standard geometries for each instance.

Parameter for Comparison	**Electronics Cooling** Composite	State of the Art	**Permafrost Retention** Composite	State of the Art
Materials Used	ABS+copper	copper	PVC+steel	steel
$k_{eff}{}'$ - β rank	1	13	2	12
$\Gamma - \beta$ rank	2	12	1	11
Max q”	8.514/unit	8.513/unit	-	-
Gross weight	250 kg	552 kg	18,605 kg	35,726 kg
Bulk material cost	$1,220	$3,910	$14,775	$29,867
Flexible design	Yes	No	Yes	No

CHAPTER 4

DESIGN OF EXPERIMENT

While it is preferred that the metal-composite interface is an elegant material science solution, for the purposes of confirming that changing adiabatic material does not reduce overall device performance [18] currently-available metal-composite interfaces (i.e. tube fittings) are used to construct the MCHPs.

Testing cylindrical heat pipes requires uniform input of heat into the evaporator section as well as a uniform method of heat rejection. In general, heat input is achieved through direct heater application, such as flexible heaters [14, 19], NiCr wire [20], or resistance heater or heater block [7, 21]. At the condenser end, several different methods of heat removal have been used, including but not limited to a custom liquid manifold [14, 21], cooling plate [19], liquid-gas calorimeter [7], or "counterflow copper coils" [20]. Each cooling method has benefits and drawbacks, however all involve a temperature-controlled fluid that is used to remove heat. Conversely, heat pipes in industry are tested by heating one end and allowing the adiabatic and condenser sections to be cooled through natural convection in ambient air. This is sufficient for reliability tests, but for accurate performance measurements the temperature of the fluid used to cool the condenser must be controlled and measured.

In designing the thermal test, attempts were made to incorporate the most effective of the individual methods. Originally, we attempted to build a custom manifold, and with

that devise a calorimeter that would measure the liquid temperature difference between the inlet and outlet. The idea was that direct fluid contact with the heat pipe would provide for the best method of heat removal. Due to the construction of the heat pipe using only mechanical seals (i.e. no welding) it became unfeasible to enclose an end of the device within a manifold. Additionally, we determined that flowrates would have to be extremely small ($\sim \mu$L/min), or temperature measurements needed to be absurdly accurate, or water could not be used. In planning to attempt these scenarios, it was decided that the requirements put undue burdens on a test setup that did not require that level of complexity.

Similar considerations were made when designing for the heat input assembly. We initially decided to use flexible heaters clamped onto the heat pipe as our heat input, however at the heat pipe outer diameters that were planned the flexible heaters did not sit flush to the surface. It was then decided to expand the size of the heat pipe from 1/4-inch tubing to 3/4-inch, however this would require more heat than the flexible heaters could provide. Ultimately the flexible heaters were replaced with a cartridge heater/calorimeter combination.

For the sake of simplicity and to normalize the test setup and provide for measurement symmetry, both the heat source and heat sink were designed with the same calorimeter block. The difference being that the heat source had through-holes drilled for the cartridge heaters, whereas the heat sink would be clamped to an off-the-shelf cold plate.

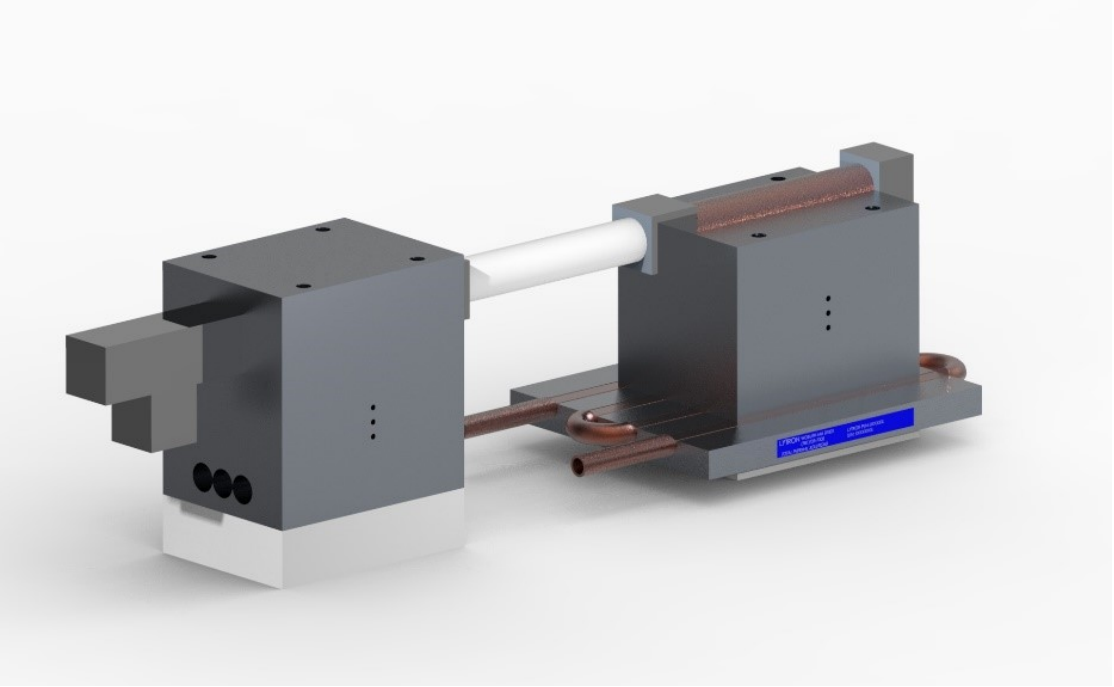

Figure 4.1: CAD image of the final iteration of thermal test setup, with the clamping block on the condenser end removed to show the heat pipe wall.

4.1 Thermal Test

For the MCHP test, a custom clamping block calorimeter was constructed. Figure 4.1 depicts how the MCHP evaporator and condenser sections are clamped inside the calorimeter block. Thermal interface material (AOS 52022JS) is spread on the outer surface of the MCHP to achieve good thermal contact with the block. Between each surface of the thermal test setup, the same TIM was used.

On the evaporator side, a heater block was machined to fit three cartridge heaters (McMaster 300W / 120V) snugly within the block. The calorimeter and top clamp, along with ceramic insulation, are bolted together with socket head screws and make up the hot end of the MCHP. On the condenser side, the calorimeter clamping blocks are secured to a cold

plate (Lytron CP12G01) and insulation using socket head cap screws. The cold plate tubes were attached to a recirculating chiller (Thermorack E02) that holds the coolant temperature constant.

Inside the calorimeter bases, three 0.1-inch diameter holes were drilled into the horizontal center of the block. One hole was 1.25 inches from the bottom surface, with the second and third holes 0.25 and 0.5 inches vertically spaced, respectively. Three thermistors (Omega TH-44006-31-T) were then inserted into these holes, forming the calorimeter. TIM was applied to each thermistor to improve the thermal contact. For proper measurement of the heat input to the heat pipe, the calorimeter must be built such that at the locations the temperatures are measured, there is 1-D heat conduction through the calorimeter.

To ensure that the calorimeter performed as required, an ANSYS simulation was performed. The outer walls of the calorimeter were insulated by providing a convection heat transfer coefficient of 1×10^{-10} W/m^{2}K. The sensitivity of the results to this insulating convective heat transfer coefficient are negligible. At the heater interface, a heat flux of 100 W/cm^2 was input to the inner walls of the through-holes, simulating cartridge heaters inserted into the block. The cutout surface had a convective heat transfer coefficient of 1000 W/cm^{2}K with a convective fluid temperature of 288 K, to represent the contact of the heat pipe drawing heat from the evaporator calorimeter. This simulation was run at steady state, and the temperatures were probed at the surfaces at the center of the calorimeter block.

Even with the near-perfect insulation, there was still roughly 23% heat lost from the heater surfaces to the evaporator surface. This indicates that it is crucial the heat not be measured using the voltage supplied to the heaters, but instead using another method

(e.g. a calorimeter). The simulation showed that at the temperatures of the inner surfaces that the thermistor probes would read have a linear temperature distribution, confirming that 1-D conduction is taking place. Additionally, it can be seen in Figure 4.2 that there is a relatively linear temperature distribution at the outer surface of the calorimeter. The temperatures indicate a heat flux that is 7.7% higher than what the heat pipe surface would receive. While this value is still larger than no difference, it is a significant improvement to just reading heater power. Additionally, were the calorimeter to be made taller, with more space between the thermistors, heater cartridges, and evaporator interface, it is predicted that this could improve the percent difference between the measured and delivered heat flux.

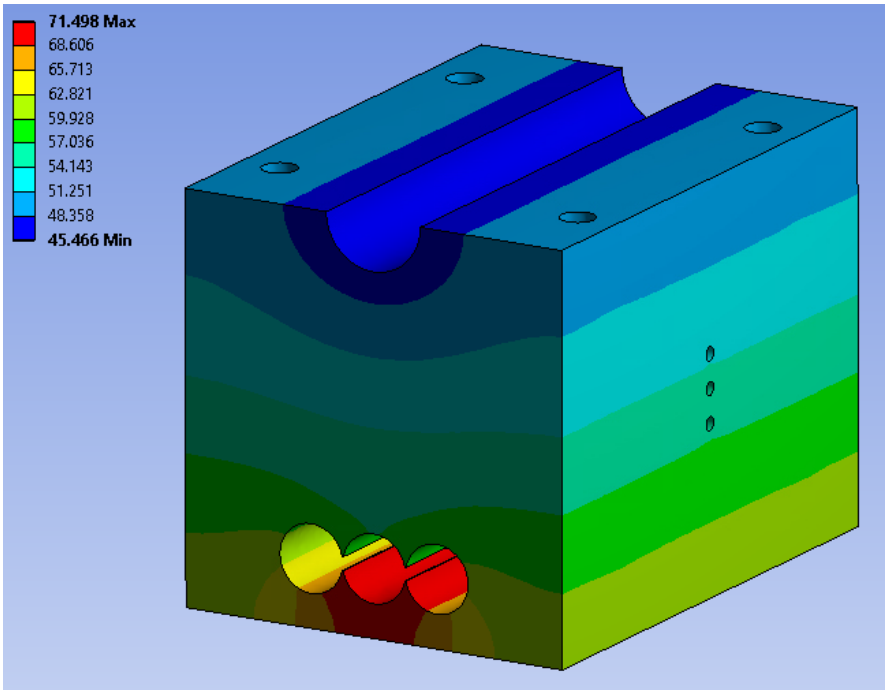

Figure 4.2: ANSYS simulation results of the evaporator calorimeter. Temperatures range from 71.498° C to 45.466° C. Internal temperatures are used to calculate the heat flux flowing from the heater surfaces to the heat pipe evaporator surface.

The assumption and further ANSYS verification was that the calorimeters provided 1-D

heat transfer. With this, the temperatures measured by the thermistors, and the distance and material thermal conductivity between each temperature, we determined the heat input to the MCHP using Fouriers Law.

4.2 Error Analysis

Error propagation occurs when measured quantities with uncertainties are used to calculate other quantities. The specific effective thermal conductivity calculation requires heat flux, which itself requires temperature and distance measurements, and temperature gradient measurements. The heat flux is determined by the calorimeter block at the evaporator. There, thermistors measure the temperature at the center of the calorimeter, and with a known material thermal conductivity, distance between each temperature, and assumed 1-D heat flow, a heat flux can be calculated. Additionally, temperature probes along the heat pipe measure the gradient, with their own uncertainty. Using these values, $k_{eff}{}'$ is calculated using Equation 3.1.

For the temperature gradient along the heat pipe, the thermistors used all had uncertainties of either ± 0.1 K or ± 0.2 K, depending on the location. The average evaporator temperature was required, so following linear combination relationship [22]

$$\delta w^2 = \delta x^2 + \delta y^2 + \delta z^2. \tag{4.1}$$

The temperatures can be substituted for the linearly-combined variables to get

$$\delta T_{evap} = \pm\sqrt{\delta {T_1}^2 + \delta {T_2}^2} = \pm\sqrt{2\delta {T_1}^2}. \tag{4.2}$$

The same calculation made for the condenser temperatures yields a total ΔT uncertainty to be

$$\delta T = \pm\sqrt{\delta T_{evap}{}^2 + \delta T_{cond}{}^2} = \pm\sqrt{2\delta T_{evap}{}^2}. \tag{4.3}$$

For the heat flux, there are two areas of propagating uncertainty to consider. The temperatures were measured with thermistors with accuracies of ± 0.1 K and the thermistor holes were drilled 0.5 inches apart with ± 0.005-inch precision. The temperature errors for the heat flux at the evaporator have uncertainties that effect the temperature difference that is of interest, ΔT_{cal}. The uncertainty of this value (δT_{cal}) can be calculated using the linear combination of the temperature differences. The average temperature gradient over the entire calorimeter is calculated using Equation 4.4.

$$\Delta T_{cal,all} = \frac{\Delta T_{cal,1} + \Delta T_{cal,2}}{2} \tag{4.4}$$

The uncertainty for this is then found using the linear combination relation again:

$$\delta\Delta T_{cal,1} = \delta\Delta T_{cal,2} = \pm\sqrt{\delta T_{cal,1}{}^2 + \delta T_{cal,2}{}^2}. \tag{4.5}$$

The uncertainty for the overall calorimeter temperature difference ($\Delta T_{cal,all}$) can be calculated using the same relationship:

$$\delta\Delta T_{cal,all} = \pm\sqrt{\delta\Delta T_{cal,1}{}^2 + \delta\Delta T_{cal,2}{}^2} = \pm\sqrt{2\delta\Delta T_{cal,1}}. \tag{4.6}$$

The uncertainty for the cross-sectional area of the calorimeter is determined using Equation 4.7:

$$\delta A = \pm A\sqrt{(\frac{\delta L}{L})^2 + (\frac{\delta W}{W})^2}, \tag{4.7}$$

where L and W are the length and width, respectively, of the calorimeter in the plane parallel to the workbench. Using precision machining with tolerances of ± 0.002 inches (± 0.05 mm) gives a propagated uncertainty of the cross-sectional area as ± 0.164 mm^2.

Finally, we assumed that there is a ± 1 W/mK uncertainty in the thermal conductivity of the calorimeter, which is machined from 6061 Aluminum that has a thermal conductivity of 167 W/mK at 298 K.

Using the calculated uncertainties, the propagated uncertainty in the calorimeter heat input measurement can be determined using Equation 4.8:

$$\delta q = \pm q\sqrt{(\frac{\delta k}{k})^2 + (\frac{\delta A}{A})^2 + (\frac{\delta \Delta T_{cal,all}}{\Delta T_{cal,all}})^2 + (\frac{\delta \Delta x}{\Delta x})^2}. \tag{4.8}$$

The final propagated uncertainty for the specific effective thermal conductivity can be calculated using a similar relationship:

$$\delta k'_{eff} = \pm k'_{eff}\sqrt{(\frac{\delta \Delta T}{\Delta T})^2 + (\frac{\delta q}{q})^2}, \tag{4.9}$$

where $\delta k'_{eff}$ is the uncertainty of the specific effective thermal conductivity.

4.3 Fabrication

Building and testing a MCHP requires methods to join and seal a metal-composite container. Introducing noncondensable gases (NCGs) into the system reduces the effectiveness and will ultimately cause the device to fail [5]. NCGs will change the pressure inside the heat pipe and cause the working fluid to cease performing at saturation [1, 4]. To avoid this, the interface between the metal and composite material must be sealed in such a way that protects the working fluid and the inside of the device from NCGs. For the purposes of the MCHP, we also wanted the device be modular and able to be taken apart.

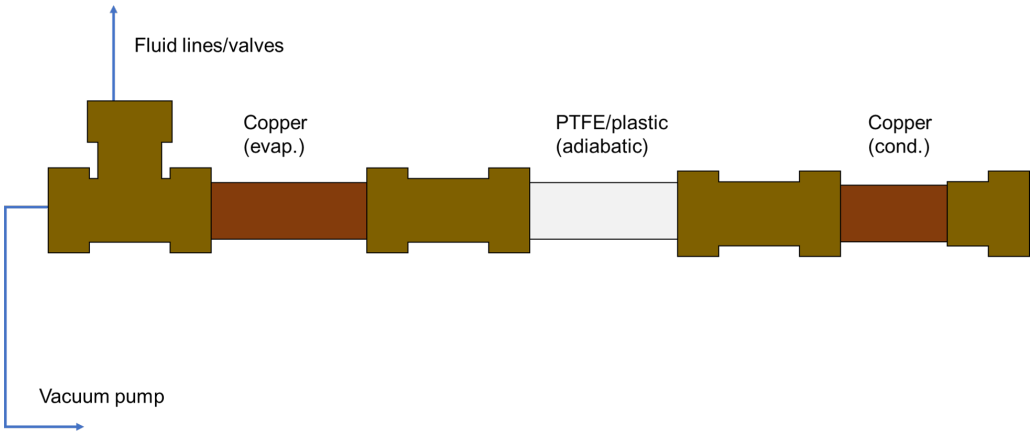

Figure 4.3: Diagram of MCHP comprising brass compression fittings, copper tubing, and PTFE tubing.

Therefore, the decision for a mechanical seal to connect the two materials was made. More specifically, compression tube fittings were used for the heat pipe wall, as shown in Figure 4.3.

Copper tubing (0.75-inch/0.032-inch OD/wall thickness) and PTFE tubing (0.75-inch/0.625-inch OD/ID) were cut to lengths such that after fittings are applied the exposed copper and PTFE lengths were 4 inches each. The parts were flushed and cleaned with Acetone, then

IPA. Each component was let dry in a chemical fume hood. After fitting the copper and PTFE tubing, a copper 100-mesh wick was double-wrapped and fit into the container. This completed the assembly of the wall-wick structure of the MCHP.

Figure 4.4 shows a simplified fluid system. The assembly consists of a cleaned pressure vessel containing the working fluid, pressure transducer (Omega PX409-015VV), and vacuum pump (Edwards RV8). These components were connected using copper and stainless-steel tubing and brass and stainless-steel compression fittings. Bellows valves were operated to provide isolation between the components and the MCHP. Each component was flushed with IPA, heated, and degassed prior to charging the heat pipe. The filling operation could begin once the MCHP structure described earlier was assembled.

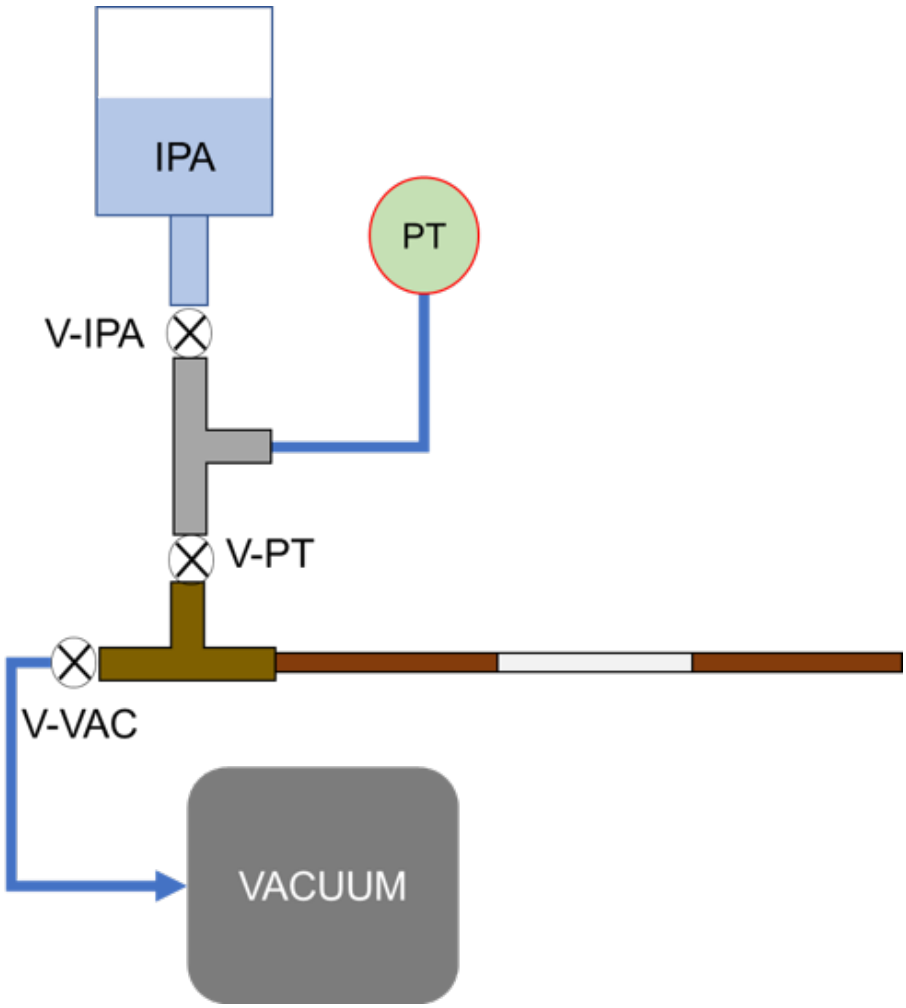

Figure 4.4: MCHP vacuum and charging assembly. This includes a vacuum pump, pressure transducer, and vacuum container with the working fluid.

The valve nearest the working fluid (V-PV) was closed, and the valves isolating the vacuum pump (V-VAC) and the pressure transducer (V-PT) were opened. The vacuum pump was then turned on and ran until the heat pipe container and all other components are degassed. This also removes all NCGs from the MCHP while also removing any that would be downstream of the working fluid. It is important that the working fluid itself if protected from the vacuum pump during this time, as the pump could be damaged by intaking liquid directly.

At this point, the chiller was turned on, cooling down the condenser end of the MCHP. This would compel all of the working fluid to condense at that end, fully wetting the wick and preventing any remaining liquid or vapor from being trapped on the wrong side of the valve.

Once vacuum is reached (-14.7 psig), the vacuum pump is isolated by closing V-VAC. At this point the container is under vacuum and sealed. Next, V-IPA is opened, drawing the liquid from the container into the heat pipe. The amount of working fluid to charge the heat pipe with is determined by the wick volume and operating conditions. Once charged, the heat pipe can be isolated from the fluid system by closing the hand valve directly above the tee fitting (V-PT). At that point, the heat pipe construction is complete.

4.4 Experimental Results

Initial results indicate that the fabrication and testing methods detailed previously work as expected. As a preliminary test of the experimental setup, a device was constructed and tested using the methods described. The experiment was run until all temperatures reached steady state. To do this, power was supplied to the heaters until temperatures approached 75° C. The power was then manually reduced and tuned to keep the calorimeter temperature reading nearest to the heaters constant. Chiller water temperature was set to 20° C. Once heat pipe wall and calorimeter temperatures reached steady state, the data was recorded.

Knowing the temperature difference inside the calorimeter, material thermal conductivity, and distance between the discrete temperatures, a heat input was calculated to be 62.76 W. This heat input was used in the validation model as the heat supplied, or Q. The model was

also adjusted to account for IPA instead of water as the working fluid. In other verification simulations, water had been used in the experimental heat pipe, so that was the working fluid used in the model. Specific heat, thermal conductivity, and latent heat of vaporization for saturated IPA were set to constants in lieu of having access to a thermophysical property database that can be called within the code.

The results of the simulation and experimental comparison are shown in Figure 4.5. Included in this figure are the error bars for the discrete temperatures measured using the thermistors. The difference between the two data sets can be described by several factors.

The heat calculated from the thermistors inside the calorimeter is less than the heat supplied to the heat pipe, as shown through the ANSYS simulation. If this $\sim$7.7% reduction is included in the model, the temperatures would agree more closely. Additionally, the experimental wall temperatures are higher than the simulation would predict. This can be explained through lack of enough insulation, higher axial conductance than previously thought, or some issues with the IPA integration of the model, which assumes constant properties for the working fluid. Future improvements to the experiment and model detailed in the following chapter could enhance agreement between the simulation and the experiment.

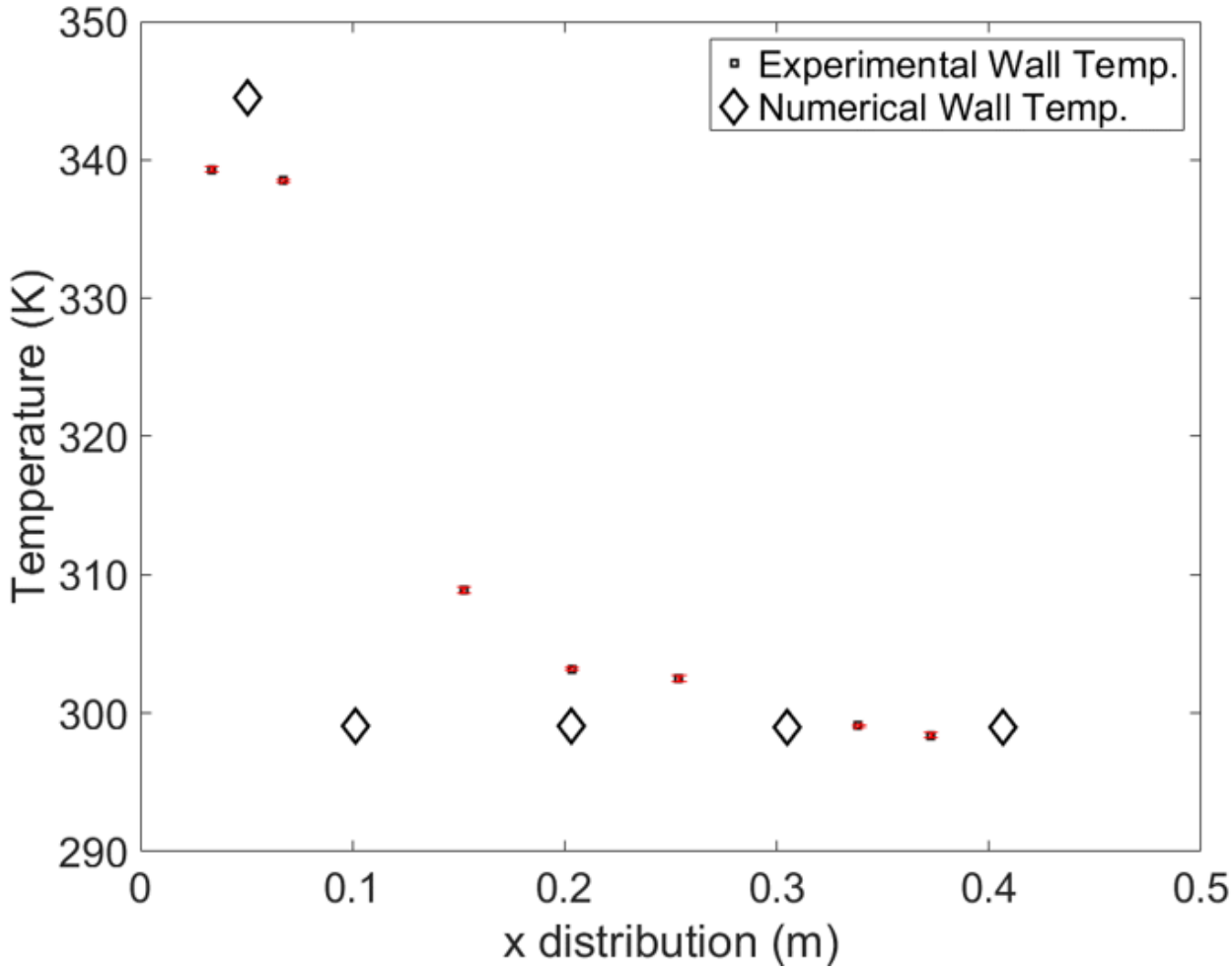

Figure 4.5: Preliminary experimentally-measured temperatures from an all-copper heat pipe compared to expected temperature profile output from the model, using IPA as working fluid for both.

CHAPTER 5

SUMMARY AND CONCLUSIONS

5.1 Summary

In this work, we have shown the MCHPs exhibit great promise in the ability to reduce cost and weight of all-metal devices without sacrificing performance. The model results combined with preliminary experiments offer insight as to how these devices will perform and how they can be constructed.

The 1-D heat pipe performance model was developed as a fast and accurate simulation of a cylindrical heat pipe. The model incorporated heat and mass transfer through the wick, liquid-vapor interfacial heat transfer, and two-phase heat transfer and combined these processes into a thermal resistance network. Wall and fluid temperatures could then be calculated using a given heat input. The heat flow through the vapor core as well as through the heat pipe wall was also calculated, confirming that very little heat is moved through axial conduction. Capillary, sonic, and physical limits were all taken into account, and heat input limits for specific heat pipe geometries were calculated. The model was used to gain insight into how specific effective thermal conductivity (i.e. mass-normalized performance) changes based on the wall material of the adiabatic section, outer radius, and lengths of the sections. The heat pipe limits were shown to be insensitive to adiabatic wall material, while

other factors, such as those listed above, directly affected these limits.

Once the validity of the idea of an MCHP was established, the model was used to test how specific materials would impact the overall cost and performance improvements. Several types of non-metal materials were simulated as adiabatic walls, and the devices were optimized based on cost, specific performance, and $k_{eff}{}'$. The results of those simulations, as well as future studies and challenges, were discussed.

To provide experimental data and enhance the findings of the model, a thermal experiment and fabrication process was designed. We built an experiment using a heater-block calorimeter that directly measured the amount of heat input to the heat pipe. With this, we built and tested a heat pipe, verifying that the system works as expected. For the preliminary data, an all-copper heat pipe was built and tested, however the experiment will test future heat pipes of both the metal and composite variety.

Modular composite heat pipes are in the nascent stage of development, and future exploration through research and industry will likely bring this technology forward quickly. Improvements in manufacturing techniques and material sciences allow for the possibility that MCHPs can be devices not found just in a lab, but also on satellites, wearable technologies, or consumer electronics.

5.2 Future Work

5.2.1 Research Areas

Although the studies here identify MCHPs as an ideal thermal management technology, more work is needed to experimentally demonstrate the concept. Three practical issues are

particularly important. The first is related to the wettability of most polymer materials. The majority of the polymers studied here are light weight, cheap, and machinable, however the non-polar nature of their molecules makes them difficult to wet for water, having typical intrinsic advancing contact angles $\theta_a > 90°$. Future work is needed to develop wettable polymer wicks that can enable capillary action and ensure the fidelity of performance for the MCHPs. A potential pathway to achieve wettable polymers is using plasma enhanced PDMS coatings [23], which have been shown to demonstrate contact angles approaching $\theta_a \sim 20°$ [23]. A secondary approach to achieve wettability would be to coat the inside of the plastic adiabatic section with a metal via electrodeposition, and then use scalable wet-etch based micro-nanostructuring techniques to create superhydrophilic coatings [24–28]. Lastly, the use of wick inserts presents a third option to monolithically connect the three sections of the composite heat pipe [19, 29, 30].

A second avenue for further research deals with the sealing of the MCHPs. All metal heat pipes are filled and sealed at one point, providing good vacuum maintenance and long-term operational fidelity. Research is needed to identify the sealing mechanism of the plastic-to-metal joints between the adiabatic and evaporator/condenser sections. Although good vacuum-tight sealing mechanisms employing deformable techniques exist (i.e. Swagelok), the added cost and weight of fittings and consistency of seals make these approaches unattractive. The capacity to utilize additive manufacturing to print the plastic adiabatic section directly on the evaporator and condenser make MCHPs particularly advantageous. Furthermore, sealing at the polymer/metal joint using molten plastic presents a good option for implementation, as this technique is currently used for glass-to-metal sealing in high vacuum

components [31]. In addition to sealing at the polymer-metal joint, vacuum compatibility of some plastics remains an issue. Table 3.1 lists the total mass losses of the plastics considered here, showing extremely elevated values for PP and PVC, with others orders of magnitude higher than metals. Many heat pipe operational conditions demand the use of sub-atmospheric conditions inside the device, with the saturation pressure approaching rough-vacuum levels ($\sim$10 kPa) [4]. If outgassing were to occur from the adiabatic material, the buildup of non-condensable gasses would heavily degrade the composite heat pipe performance at the locations where phase change occurs [5].

A third difficulty for implementation is the reliability of the final device. Thermomechanical stresses at the plastic-to-metal interfaces during transient operation present areas for potential failure due to coefficient of thermal expansion (CTE) mismatch between the dissimilar materials. As such, more work is needed for the selection of polymer materials with well-matched CTE to metallic materials such as copper. Indeed, CTE matched polymer-metal composites are currently widely used in polychlorinated biphenyl (PCB) printed circuit board technology [32], and should be analyzed further as ideal real-life implementation materials for composite heat pipes.

Solutions of the above hurdles would facilitate the use of MCHPs while harnessing their significant weight and cost reduction at minimal cost to performance. This presents a unique device platform for next generation thermal management. Furthermore, with the advent of additive manufacturing of plastic materials (3D printing), MCHPs offer unparalleled design freedom and potential mechanical flexibility for integration into platforms previously not possible. The modeling and optimization work developed here presents a design framework

for the development of MCHPs for thermal applications ranging from the micro to macro scale.

5.2.2 Experiments

There are several avenues for future experimental studies. These include improved working fluid wetting on the composite material used in the MCHP, improved thermal test setup, and adjustments/validation improvements to the mathematical model, among others.

Currently the most expedient method of building a working MCHP requires the use of a homogeneous copper wick tightly fitted into the modular tube structure. In practice this works well, however to maximize the performance improvements of the MCHP, as well as increasing the modularity, a more ideal scenario would involve a more elegant and functional solution. Current fabrication methods used for this study were not able to devise such a method, however additive manufacturing and other improved fabrication techniques could provide them through the previously-mentioned new avenues of study.

The thermal test setup, while operational, has room for improvement. First, the heater cartridges are currently massively overpowered, which leads to loss of fine-tuning the heat input. Along those lines, the control for the power input is currently an off-the-shelf power converter with a single knob that controls the voltage output. A temperature controller, probably in concert with a solid-state relay, should be employed, both as a protection against over-heating the thermistors and for easier operation. Second, the thermistors currently have an accuracy of ± 0.1 K. This could possibly be improved by using higher-quality temperature sensors, or by making the spacing between them larger. This would increase the tempera-

ture difference in the calorimeter and reduce the uncertainty of the heat flux measurement. Finally, the entire test setup should be insulated much better than it is currently. This will reduce heat loss to the environment and hopefully decrease the uncertainty of the effective thermal conductivity measurements.

5.2.3 Modeling

The mathematical model was tested against a specific experimental study [14], however further validation is necessary. The working fluid information in the model should be updated to reflect the MCHP currently tested. Temperature-dependent relationships governing the thermophysical properties should also be included in the model (currently this is only the case for water). This will lead to a simulation more grounded in measured data and less in hard-coded constants. Finally, once the MCHP is consistently operating as expected, the measured wall temperatures can be compared to the model results, and corrections to the model can be made to more accurately reflect what is happening physically.

REFERENCES

[1] A. Faghri, "Heat pipes: review, opportunities and challenges," *Frontiers in Heat Pipes (FHP)*, vol. 5, no. 1, 2014.

[2] M. G. Mwaba, X. Huang, and J. Gu, "Influence of wick characteristics on heat pipe performance," *International journal of energy research*, vol. 30, no. 7, pp. 489–499, 2006.

[3] S. Sorensen, J. Smith, and J. Zarling, "Thermal performance of taps heat pipes with non condensable gas blockage," in *Cold Regions Engineering: Cold Regions Impacts on Transportation and Infrastructure*, 2002, pp. 1–12.

[4] D. Reay, R. McGlen, and P. Kew, *Heat pipes: theory, design and applications*. Butterworth-Heinemann, 2013.

[5] A. Faghri, "Review and advances in heat pipe science and technology," *Journal of heat transfer*, vol. 134, no. 12, p. 123001, 2012.

[6] T. L. Bergman, F. P. Incropera, D. P. DeWitt, and A. S. Lavine, *Fundamentals of heat and mass transfer*. John Wiley & Sons, 2011.

[7] G. Hwang, M. Kaviany, W. Anderson, and J. Zuo, "Modulated wick heat pipe," *International Journal of Heat and Mass Transfer*, vol. 50, no. 7-8, pp. 1420–1434, 2007.

[8] S. Chavan, H. Cha, D. Orejon, K. Nawaz, N. Singla, Y. F. Yeung, D. Park, D. H. Kang, Y. Chang, Y. Takata et al., "Heat transfer through a condensate droplet on hydrophobic and nanostructured superhydrophobic surfaces," *Langmuir*, vol. 32, no. 31, pp. 7774–7787, 2016.

[9] J. W. Rose, "Accurate approximate equations for intensive sub-sonic evaporation," *International journal of heat and mass transfer*, vol. 43, no. 20, pp. 3869–3875, 2000.

[10] Z. Lu, S. Narayanan, and E. N. Wang, "Modeling of evaporation from nanopores with nonequilibrium and nonlocal effects," *Langmuir*, vol. 31, no. 36, pp. 9817–9824, 2015.

[11] D. Labuntsov and A. Kryukov, "Analysis of intensive evaporation and condensation," *International Journal of Heat and Mass Transfer*, vol. 22, no. 7, pp. 989–1002, 1979.

[12] J. Barrett and C. Clement, "Kinetic evaporation and condensation rates and their coefficients," *Journal of colloid and interface science*, vol. 150, no. 2, pp. 352–364, 1992.

[13] N. Miljkovic and E. N. Wang, "Modeling and optimization of hybrid solar thermoelectric systems with thermosyphons," *Solar Energy*, vol. 85, no. 11, pp. 2843–2855, 2011.

[14] A. Faghri and M. Buchko, "Experimental and numerical analysis of low-temperature heat pipes with multiple heat sources," *Journal of Heat Transfer*, vol. 113, no. 3, pp. 728–734, 1991.

[15] W. A. Campbell Jr, R. S. Marriott, and J. J. Park, "Outgassing data for selecting spacecraft materials," 1984.

[16] B. Richard, D. Pellicone, and W. Anderson, "Loop heat pipe wick fabrication via additive manufacturing." 47th International Conference on Environmental Systems, 2017.

[17] C. E. Heuer, "The application of heat pipes on the trans-alaska pipeline," COLD REGIONS RESEARCH AND ENGINEERING LAB HANOVER NH, Tech. Rep., 1979.

[18] K. Coulson, S. Sinha, and N. Miljkovic, "Analysis of modular composite heat pipes," *International Journal of Heat and Mass Transfer*, vol. 127, pp. 1198–1207, 2018.

[19] C. Yang, C. Song, W. Shang, P. Tao, and T. Deng, "Flexible heat pipes with integrated bioinspired design," *Progress in Natural Science: Materials International*, vol. 25, no. 1, pp. 51–57, 2015.

[20] N. Kosowski and R. Kosson, "Experimental performance of grooved heat pipes at moderate temperatures," in *6th Thermophysics Conference*, 1971, p. 409.

[21] A. B. Solomon, K. Ramachandran, and B. Pillai, "Thermal performance of a heat pipe with nanoparticles coated wick," *Applied Thermal Engineering*, vol. 36, pp. 106–112, 2012.

[22] C. J. Oshman, "Development, fabrication, and experimental study of flat polymer micro heat pipes," 2012.

[23] S. H. Tan, N.-T. Nguyen, Y. C. Chua, and T. G. Kang, "Oxygen plasma treatment for reducing hydrophobicity of a sealed polydimethylsiloxane microchannel," *Biomicrofluidics*, vol. 4, no. 3, p. 032204, 2010.

[24] K.-H. Chu, Y. Soo Joung, R. Enright, C. R. Buie, and E. N. Wang, "Hierarchically structured surfaces for boiling critical heat flux enhancement," *Applied Physics Letters*, vol. 102, no. 15, p. 151602, 2013.

[25] K.-H. Chu, Y. Zhu, N. Miljkovic, Y. Nam, R. Enright, and E. Wang, "Enhanced boiling heat transfer with copper oxide hierarchical surfaces," in *Solid-State Sensors, Actuators and Microsystems (TRANSDUCERS & EUROSENSORS XXVII), 2013 Transducers & Eurosensors XXVII: The 17th International Conference on.* IEEE, 2013, pp. 2272–2275.

[26] M. McCarthy, K. Gerasopoulos, S. C. Maroo, and A. J. Hart, "Materials, fabrication, and manufacturing of micro/nanostructured surfaces for phase-change heat transfer enhancement," *Nanoscale and Microscale Thermophysical Engineering*, vol. 18, no. 3, pp. 288–310, 2014.

[27] M. M. Rahman, E. Olceroglu, and M. McCarthy, "Role of wickability on the critical heat flux of structured superhydrophilic surfaces," *Langmuir*, vol. 30, no. 37, pp. 11 225–11 234, 2014.

[28] Y. Nam and Y. S. Ju, "A comparative study of the morphology and wetting characteristics of micro/nanostructured cu surfaces for phase change heat transfer applications," *Journal of Adhesion Science and Technology*, vol. 27, no. 20, pp. 2163–2176, 2013.

[29] C. Oshman, B. Shi, C. Li, R. Yang, Y. Lee, G. Peterson, and V. M. Bright, "The development of polymer-based flat heat pipes," *Journal of Microelectromechanical Systems*, vol. 20, no. 2, pp. 410–417, 2011.

[30] C. Oshman, B. Shi, C. Li, R. Yang, Y. Lee, and V. Bright, "Fabrication and testing of a flat polymer micro heat pipe," in *Solid-State Sensors, Actuators and Microsystems Conference, 2009. TRANSDUCERS 2009. International*. IEEE, 2009, pp. 1999–2002.

[31] J. A. Pask, "New techniques in glass-to-metal sealing," *Proceedings of the IRE*, vol. 36, no. 2, pp. 286–289, 1948.

[32] C. Zweben, "Advances in composite materials for thermal management in electronic packaging," *Jom*, vol. 50, no. 6, pp. 47–51, 1998.

APPENDIX - RAW MODELS

Included in this Appendix are the different MATLAB codes that make up the models used for the parametric sweep, sensitivity analysis, and multi-objective optimization, in that order.

```
%% Heat Pipe model grooved wick - parametric
%
%
clc; beep off; close all;clear;
set(0,'defaultfigurecolor','w'); set(0,'defaultlinelinewidth',2);
set(0,'defaultAxesFontName', 'Arial'); set(0,'DefaultAxesFontSize',24)
% FigHandle = figure (1);
%   set(FigHandle, 'Position', [100, 100, 1049, 695]);
FigHandle = figure (2);
  set(FigHandle, 'Position', [100, 100, 1049, 695]);
% FigHandle = figure (3);
%   set(FigHandle, 'Position', [100, 100, 1049, 695]);


% Copper
rhoCu= 8960;                % kg/m^3        [density of copper]
kCu  = 397;                 % W/mK          [conductivity of Cu]
% Polypropylene
rhoPl= 900;                 % kg/m^3        [density]
kPl  = 0.2;                 % W/mK          [thermal conductivity]
% Water
kl   = 0.65;                % W/mK          [conductivity of H2O
uH2Ol= 1.00e-3;             % Pa*s          [viscosity of liquid H2O] *
```

```
uH2Ov= 1.23e-5;              % Pa*s          [viscosity of vapor H2O] *


%% Comparison


%% Changing Adiabatic material
 for kAd = [kCu kPl]
    if kAd == kCu
        rhoAd = rhoCu;
        face = 'k';
        w = 1000;
    else
        rhoAd = rhoPl;
        face = 'w';
        w = 500;
    end
%% Changing geometry
% testvector = [0.05 0.15 0.3]
% testvector = [5 10 25]
testvector = [0.005 0.008 0.012]
for wL = testvector
    r_o = wL;
    if wL == testvector(1)
```

```
        edge = 'r';
    elseif wL == testvector(2)
        edge = 'g';
    else
        edge = 'b';
    end


for l_C = 0.05:0.05:0.8
dPc         = 1;
dPt         = 0;
Q           = 10;
heatflux    = 10;
uratio      = 0;
while dPc > dPt && uratio < 0.3 && heatflux < 1000 && Q < 10000
   ms   = r_o*w;
l_E     = 5*r_o;            % m             [Evaporator length] 5
l_A     = 50*r_o;           % m             [Adiabatic length] 50
% l_C     = 23.6*r_o;         % m             [Condenser length] 23.6
twick   = 0.056*r_o;        % m             [wick thickness] 0.056
twall   = 0.134*r_o;        % m             [wall thickness] 0.134
r_n     = r_o-twall;        % m             [wick outer radius]
r_i     = r_n-twick;        % m             [wick inner radius]
```

```
Q = heatflux*2*pi*r_o*l_E/(10^-4);


Twn     = ones(1,5);

Twdiff  = 1;

Qin     = Q;


%% Inputs ---------------------------------------------------------------


Tc   = 348;                % K             [condenser wall temperature]

e    = 0.50;               % void fraction [Volume fluid/Volume wick]

wss  = 0.20;               % spheres*      [ws*; N = 24]

wg   = 1.1e-3;             % m             [width of channels]

ws   = wss*wg/(1 - wss);   % m             [fin thickness]

%% Properties -----------------------------------------------------------

kl   = 0.60;               % W/mK          [conductivity of H2O

kCu  = 400;                % W/mK          [conductivity of Cu]

K    = 5.68e-12;           % m^2           [wick permeability, from Hwang]

hfg  = 2257e3;             % J/kg          [initial latent heat of H2O]

kB   = 1.38e-23;           % m^2kg/s^2/K   [Boltzmann Constant]

uH2Ol= 1.00e-3;            % Pa*s          [viscosity of liquid H2O] *

uH2Ov= 1.23e-5;            % Pa*s          [viscosity of vapor H2O] *
```

```
M    = 18.02;              % g/mol         [molar mass of H2O]

R    = 8.314;              % J/K/mol       [Gas constant]

N    = floor(2*pi*r_n/(wg + ws));

                           % number of channels


%% Initial calculations ----------------------------------------------------

l_eff= l_A + (l_E + l_C)/2; % m             [effective length]



ee      = 2*r_i/(2*r_i + ws);

kwickr   = kCu*(1-ee*(1-kl/kCu));

                           % W/mK          [conductivity of wick at condenser]

RwallE  = log(r_o/r_n)/(2*pi*l_E*kCu);

                           % K/W           [Evaporator wall resistance]

RwallC  = log(r_o/r_n)/(2*pi*l_C*kCu);

                           % K/W           [Condenser wall resistance]

RwickE  = (1-pi/4)/(2*kl*l_E*N);

                           % K/W           [Evaporator wick resistance]

RwickC  = log(r_n/r_i)/(2*pi*l_C*kwickr);

                           % K/W           [Condenser wick resistance]

kwicka  = kwickr;

Rwicka  = @(l) l/((r_n^2 - r_i^2)*pi*kwicka);
```

```
Rwalla  = @(l) l/((r_o^2 - r_n^2)*pi*kAd);
mdot    = Q/hfg;            % kg/s          [mass flow rate]
qdot    = Q/(l_E*2*pi*r_o); % W/m^2         [heat flux]
%% Temperature and Pressure Calculations ---------------------------------


T(1)    = Tc;                           % set point
T(2)    = Q*(RwallC + RwickC) + T(1);   % liquid/vapor interface temperature
    T2C = T(2) - 273;                   % T(2) in Celcius
Pl(1)   = [0.61121*exp((18.678 - T2C/234.5)*(T2C/(257.14 + T2C)))]*10^3;
                                        % condenser saturation pressure, Buck
                                        % equation (Pa)
Pv(1)   = Pl(1) - qdot/(hfg*sqrt(M/(2*pi*kB*T(2))));
                                        % PVC
    vg      = XSteam('vL_T',T2C);
    a       = 0.5;
    hiC     = 2*a/(2-a)*1/sqrt(2*pi*R*T2C)*(XSteam('hL_T',T2C)*10^3)^2/vg/T2C;
    RiC     = 1/hiC/(2*r_i*pi*l_C);     % Interface resistance
T(3)    = T(2) + Q*RiC;                 % TVC
    T3C = T(3) - 273;
dPv(1)  = -4/pi^2*(mdot^2/(8*XSteam('rhoV_T',T3C)*r_i^4));
                                        % delta Pv over condenser
dTv(1)  = R*T(3)^2/((XSteam('hV_T',T3C))*Pv(1));
```

```
                                        % delta Tv over condenser
T(4)    = T(3) + dTv(1);                % Tv at condenser/adiabatic
    T4C = T(4) - 273;
Pv(2)   = Pv(1) + dPv(1);               % Pv at condenser/adiabatic
dPv(2)  = 8*uH2Ov*mdot*l_A/(XSteam('rhoV_T',T4C)*pi*r_i^4);
                                        % delta Pv over adiabatic
dTv(2)  = R*(T(4))^2/((XSteam('hV_T',T4C))*Pv(2));
                                        % delta Tv over adiabatic
T(5)    = T(4) + dTv(2);                % Tv at adiabatic/evaporator
    T5C = T(5) - 273;
Pv(3)   = Pv(2) + dPv(2);               % Pv at adiabatic/evaporator
dPv(3)  = mdot^2/(8*XSteam('rhoV_T',T5C)*r_i^4);
                                        % delta Pv over evaporator
dTv(3)  = R*T(5)^2/((XSteam('hV_T',T5C))*Pv(3));
                                        % delta Tv over evaporator
T(6)    = T(5) + dTv(3);                % Tv at evaporator
    T6C = T(6) - 273;
Pv(4)   = Pv(3) + dPv(3);               % Pv at evaporator
                                        % delta Pl over length of heat pipe
    vg      = XSteam('vV_T',T6C);
    a       = 0.5;
    hiE     = 2*a/(2-a)*1/sqrt(2*pi*R*T6C)*(XSteam('hV_T',T6C)*10^3)^2/vg/T6C;
```

```
    RiE     = 1/hiE/(2*r_i*pi*l_E);     % Interface resistance
T(7)    = T(6) - Q*RiE;                 % liquid/vapor interface temperature
T(8)    = Q*(RwallE + RwickE) + T(7);   % evaporator wall temperature
dPl     = 8*uH2Ol*(l_E+l_A+l_C)*mdot/((XSteam('rhoL_T',((T(7)+T(2))...
/2-273))*N*pi*(2*r_i)^4));
Pl(2)   = Pl(1) - dPl;                  % Pl at evaporator
Ra(1)   = ((1/Rwicka(l_C)) + (1/Rwalla(l_C)))^-1;
Ra(2)   = ((1/Rwicka(l_A/2)) + (1/Rwalla(l_A/2)))^-1;
Ra(3)   = Ra(2);
Ra(4)   = ((1/Rwicka(l_E*2)) + (1/Rwalla(l_E*2)))^-1;
Rhp     = (T(7) - T(2))/(Q);
Qa      = Qin*(1/sum(Ra) + 1/Rhp)^-1/sum(Ra);
% Qb      = (Rhp)/(sum(Ra) + Rhp)*Q;
%% Wall temperature profile ------------------------------------------------


Tw      = Twn;
Twn(5)  = T(8);
Twn(1)  = T(1);
i = 2;
while i < length(Twn)
    Twn(i) = Twn(i-1) + Ra(i-1)*Qa;
    i = i + 1;
```

```
end

Twdiff  = Twn - Tw;

Q = Qin - Qa;

T           = fliplr(T);                % sets the evaporator at x = 0

Pv          = fliplr(Pv);

Pl          = fliplr(Pl);

Pvxdistr    = [0 l_E l_E+l_A l_E+l_A+l_C];

Tvxdistr    = Pvxdistr;

Tvplot      = [T(3) T(4) T(5) T(6)];

Pvplot      = Pv;


keff        = Qin/(T(1) - T(8))*(l_E+l_A+l_C);

    massa   = (l_A)*pi*(r_o^2-r_i^2)*rhoAd;

    masse   = (l_E)*pi*(r_o^2-r_i^2)*rhoCu;

    massc   = (l_C)*pi*(r_o^2-r_i^2)*rhoCu;

    masst   = massa+masse+massc;

    keffp   = keff/masst;

Tdrop       = T(1) - T(8);


%% Stopping parameters

u           = Q/(pi*r_i^2)/XSteam('rhoV_T',mean(Tvplot)-273)/hfg;

                            % m/s       [vapor velocity]
```

```
Rev         = XSteam('rhoV_T',mean(Tvplot)-273)*u*2*r_i...
/XSteam('my_pT',mean(Pv)/100000,mean(Tvplot)-273);
                            % --        [vapor Reynolds number]
c           = XSteam('wV_T',mean(Tvplot)-273);
                            % m/s       [vapor speed of sound]
uratio      = u/c;          % ratio to determine if limit is hit
heatflux = heatflux + 10;
dPc     = 2*78.2e-3/(wg/2);            % Capillary pressure limit of grooves
dPvt    = Pv(4) - Pv(1);                % Vapor pressure drop
dPt     = dPvt + dPl;                   % Total pressure drop
end
fprintf('keff = %3.2f\nHeat flux = %3.2f W/cm^2\n',keffp,heatflux)
fprintf('Tdrop = %3.2f\nQ = %3.2f\n',Tdrop,Q)
fprintf('dPc = %3.2f\ndPl = %3.2f\n',dPc,dPl)
fprintf('variable = %3.3f\n\n',l_A)


f2=figure (2);
hold on
box on
plot(l_C,keffp,'Marker','o',...
'MarkerFaceColor',face,...
'MarkerSize',ms,...
```

```
'MarkerEdgeColor',edge)

xlabel('L_C (m)')

ylabel('spec. k_e_f_f (W/mK/kg)')

drawnow


end

end


end

%% Saving figures

saveas(f2,'xsection_LC_ro_keffp.png');

% saveas(f2,'twickRvsKeffp.png');

% saveas(f3,'twickRvsKoverdT.png');
```

```
%% Heat Pipe model grooved wick - sensitivity
%
%
clc; beep off; close all;clear;
set(0,'defaultfigurecolor','w'); set(0,'defaultlinelinewidth',2);
set(0,'defaultAxesFontName', 'Arial'); set(0,'DefaultAxesFontSize',24)
FigHandle = figure (1);
  set(FigHandle, 'Position', [100, 100, 1049, 695]);
% FigHandle = figure (2);
%   set(FigHandle, 'Position', [100, 100, 1049, 695]);
FigHandle = figure (3);
  set(FigHandle, 'Position', [100, 100, 1049, 695]);
s = 1;
dPc  = 1;
dPt  = 0;
Q    = 500;
% Copper
rhoCu= 8960;                % kg/m^3        [density of copper]
kCu  = 397;                 % W/mK          [conductivity of Cu]
% Polypropylene
rhoPl= 900;                 % kg/m^3        [density]
kPl  = 0.2;                 % W/mK          [thermal conductivity]
```

```
% Water
kl   = 0.65;                % W/mK          [conductivity of H2O
uH2Ol= 1.00e-3;             % Pa*s          [viscosity of liquid H2O] *
uH2Ov= 1.23e-5;             % Pa*s          [viscosity of vapor H2O] *


%% Changing Adiabatic material
kAd = kPl;
rhoAd = rhoCu;
w = 1000;
%% HERE MUST CHOOSE WHAT VARIABLE TO CHANGE
for l_C = 0.05:0.01:0.5
r_o     = 0.005;             % m
   ms   = r_o*w;
l_A     = 50*r_o;           % m             [Adiabatic length] 50
l_E     = 5*r_o;            % m             [Evaporator length] 5
% l_C     = 23.6*r_o;         % m             [Condenser length] 23.6
twick   = 0.056*r_o;        % m             [wick thickness] 0.056
twall   = 0.134*r_o;        % m             [wall thickness] 0.134
r_n     = r_o-twall;        % m             [wick outer radius]
r_i     = r_n-twick;        % m             [wick inner radius]


T       = ones(1,8);
```

```
Twn     = ones(1,5);

Twdiff  = 1;

Qin     = Q;

dPc  = 1;

dPt  = 0;


%% Inputs


Tc   = 348;                % K             [condenser wall temperature]

e    = 0.50;               % void fraction [Volume fluid/Volume wick]

N    = 23;

% wss  = 0.20;               % spheres*      [ws*; N = 24]

wg   = 1.1e-3;             % m             [width of channels]

wss  = 1-N*wg/2/pi/r_n;    % spheres*      [ws*; N = variable]

ws   = wss*wg/(1 - wss);   % m             [fin thickness]

%% Properties

kl   = 0.60;               % W/mK          [conductivity of H2O

kCu  = 400;                % W/mK          [conductivity of Cu]

K    = 5.68e-12;           % m^2           [wick permeability, from Hwang]

hfg  = 2257e3;             % J/kg          [initial latent heat of H2O]

kB   = 1.38e-23;           % m^2kg/s^2/K   [Boltzmann Constant]

uH2Ol= 1.00e-3;            % Pa*s          [viscosity of liquid H2O] *
```

```
uH2Ov= 1.23e-5;             % Pa*s          [viscosity of vapor H2O] *

M    = 18.02;               % g/mol         [molar mass of H2O]

R    = 8.314;               % J/K/mol       [Gas constant]

% N    = 2*pi*r_n/(wg + ws);

                            % number of channels


%% Initial calculations

l_eff= l_A + (l_E + l_C)/2; % m             [effective length]



ee      = 2*r_i/(2*r_i + ws);

kwickr   = kCu*(1-ee*(1-kl/kCu));

                            % W/mK          [conductivity of wick at condenser]

RwallE  = log(r_o/r_n)/(2*pi*l_E*kCu);

                            % K/W           [Evaporator wall resistance]

RwallC  = log(r_o/r_n)/(2*pi*l_C*kCu);

                            % K/W           [Condenser wall resistance]

RwickE  = (1-pi/4)/(2*kl*l_E*N);

                            % K/W           [Evaporator wick resistance]

RwickC  = log(r_n/r_i)/(2*pi*l_C*kwickr);

                            % K/W           [Condenser wick resistance]

kwicka  = kwickr;
```

```
Rwicka  = @(l) l/((r_n^2 - r_i^2)*pi*kwicka);

Rwalla  = @(l) l/((r_o^2 - r_n^2)*pi*kAd);

mdot    = Q/hfg;            % kg/s          [mass flow rate]

qdot    = Q/(l_E*2*pi*r_o); % W/m^2         [heat flux]

%% Temperature and Pressure Calculations

T(1)    = Tc;                           % set point

T(2)    = Q*(RwallC + RwickC) + T(1);   % liquid/vapor interface temperature

    T2C = T(2) - 273;                   % T(2) in Celcius

Pl(1)   = [0.61121*exp((18.678 - T2C/234.5)*(T2C/(257.14 + T2C)))]*10^3;

                                        % condenser saturation pressure, Buck

                                        % equation (Pa)

Pv(1)   = Pl(1) - qdot/(hfg*sqrt(M/(2*pi*kB*T(2))));

                                        % PVC

    vg      = XSteam('vL_T',T2C);

    a       = 0.5;

    hiC     = 2*a/(2-a)*1/sqrt(2*pi*R*T2C)*(XSteam('hL_T',T2C)*10^3)^2/vg/T2C;

    RiC     = 1/hiC/(2*r_i*pi*l_C);     % Interface resistance

T(3)    = T(2) + Q*RiC;                 % TVC

    T3C = T(3) - 273;

dPv(1)  = -4/pi^2*(mdot^2/(8*XSteam('rhoV_T',T3C)*r_i^4));

                                        % delta Pv over condenser

dTv(1)  = R*T(3)^2/((XSteam('hV_T',T3C))*Pv(1));
```

```
                                        % delta Tv over condenser
T(4)    = T(3) + dTv(1);                % Tv at condenser/adiabatic
    T4C = T(4) - 273;
Pv(2)   = Pv(1) + dPv(1);               % Pv at condenser/adiabatic
dPv(2)  = 8*uH2Ov*mdot*l_A/(XSteam('rhoV_T',T4C)*pi*r_i^4);
                                        % delta Pv over adiabatic
dTv(2)  = R*(T(4))^2/((XSteam('hV_T',T4C))*Pv(2));
                                        % delta Tv over adiabatic
T(5)    = T(4) + dTv(2);                % Tv at adiabatic/evaporator
    T5C = T(5) - 273;
Pv(3)   = Pv(2) + dPv(2);               % Pv at adiabatic/evaporator
dPv(3)  = mdot^2/(8*XSteam('rhoV_T',T5C)*r_i^4);
                                        % delta Pv over evaporator
dTv(3)  = R*T(5)^2/((XSteam('hV_T',T5C))*Pv(3));
                                        % delta Tv over evaporator
T(6)    = T(5) + dTv(3);                % Tv at evaporator
    T6C = T(6) - 273;
Pv(4)   = Pv(3) + dPv(3);               % Pv at evaporator
                                        % delta Pl over length of heat pipe
    vg      = XSteam('vV_T',T6C);
    a       = 0.5;
    hiE     = 2*a/(2-a)*1/sqrt(2*pi*R*T6C)*(XSteam('hV_T',T6C)*10^3)^2/vg/T6C;
```

```
    RiE     = 1/hiE/(2*r_i*pi*l_E);     % Interface resistance
T(7)    = T(6) - Q*RiE;                 % liquid/vapor interface temperature
T(8)    = Q*(RwallE + RwickE) + T(7);   % evaporator wall temperature
dPl     = 8*uH2Ol*(l_E+l_A+l_C)*mdot...
/((XSteam('rhoL_T',((T(7)+T(2))/2-273))*N*pi*(2*r_i)^4));
Pl(2)   = Pl(1) - dPl;                  % Pl at evaporator
Ra(1)   = ((1/Rwicka(l_C)) + (1/Rwalla(l_C)))^-1;
Ra(2)   = ((1/Rwicka(l_A/2)) + (1/Rwalla(l_A/2)))^-1;
Ra(3)   = Ra(2);
Ra(4)   = ((1/Rwicka(l_E*2)) + (1/Rwalla(l_E*2)))^-1;
Rhp     = (T(7) - T(2))/(Q);
Qa      = Qin*(1/sum(Ra) + 1/Rhp)^-1/sum(Ra);
% Qb      = (Rhp)/(sum(Ra) + Rhp)*Q;
%% Wall temperature profile


Tw      = Twn;
Twn(5)  = T(8);
Twn(1)  = T(1);
i = 2;
while i < length(Twn)
    Twn(i) = Twn(i-1) + Ra(i-1)*Qa;
    i = i + 1;
```

```
end

Twdiff  = Twn - Tw;

Q = Qin - Qa;

T           = fliplr(T);                % sets the evaporator at x = 0

Pv          = fliplr(Pv);

Pl          = fliplr(Pl);

Pvxdistr    = [0 l_E l_E+l_A l_E+l_A+l_C];

Tvxdistr    = Pvxdistr;

Tvplot      = [T(3) T(4) T(5) T(6)];

Pvplot      = Pv;


keff        = Qin/(T(1) - T(8))*(l_E+l_A+l_C);

    massa   = (l_A)*pi*(r_o^2-r_i^2)*rhoAd;

    masse   = (l_E)*pi*(r_o^2-r_i^2)*rhoCu;

    massc   = (l_C)*pi*(r_o^2-r_i^2)*rhoCu;

    masst   = massa+masse+massc;

    keffp   = keff/masst;

Tdrop       = T(1) - T(8);

%%%%%%%%%%%%%%%%%%%%%%%%%%%%%%%%%%%%%%%%%%%%%%%%%%%%%%%%%%%%%%%%

%% Setting up Sensitivity plots and checking limits

fig1=figure (1);

hold on
```

```
box on

p1=plot(l_C,keffp,'Marker','o',...

'MarkerFaceColor','w','MarkerSize',ms,'MarkerEdgeColor','k');

xlabel('L_C (m)')

ylabel('spec. k_e_f_f (W/mK/kg)')


u           = Q/(pi*r_i^2)/XSteam('rhoV_T',mean(Tvplot)-273)/hfg;

Rev         = XSteam('rhoV_T',mean(Tvplot)-273)*u*2*r_i...

/XSteam('my_pT',mean(Pv)/100000,mean(Tvplot)-273);

c           = XSteam('wV_T',mean(Tvplot)-273);

uratio      = u/c;

heatflux    = qdot*10^-4;

% fprintf('keff = %3.2f\nHeat flux = %3.2f W/cm^2\n',keff,heatflux)

% fprintf('Tdrop = %3.2f\nQ = %3.2f\n',Tdrop,Q)

% fprintf('dPc = %3.2f\ndPl = %3.2f\n',dPc,dPl)

% fprintf('variable = %3.8f\n\n',uratio)


%% Sensitivity

sensvar         = l_C;

dsensvar        = keffp;


variable(s)     = sensvar;
```

```
depvariable(s)  = dsensvar;

variablel(s)    = log10(sensvar);

depvariablel(s) = log10(dsensvar);

s = s+1;

end

f1 = polyfit(variable,depvariable,3);

f1l = polyfit(variablel,depvariablel,3);

p2=plot(variable,polyval(f1,variable),'b');

legend([p1 p2],'calculated','fitted')

hold off

fig3=figure(3);

df1= polyder(f1l);

plot(variable,polyval(df1,variablel))

xlabel('L_C (m)')

ylabel('Sensitivity on: spec. k_e_f_f')

% R^2 value

yfit=polyval(f1l,variablel);

yresid=depvariablel-yfit;

SSresid=sum(yresid.^2);

SStotal=(length(depvariablel)-1)*var(depvariablel);

rsq = 1-SSresid/SStotal;
```

```
%% Heat Pipe model grooved wick - Monte Carlo
%
%
%
%% Initial Settings
if parpool('local') < 2
    set (findResource(), 'ClusterSize', 2);
    parpool close force;
    parpool open 2;
end
clc; beep off; close all;clear;
set(0,'defaultfigurecolor','w'); set(0,'defaultlinelinewidth',2);
set(0,'defaultAxesFontName', 'Arial'); set(0,'DefaultAxesFontSize',24)
FigHandle = figure (1);
  set(FigHandle, 'Position', [100, 100, 1049, 695]);
FigHandle = figure (2);
  set(FigHandle, 'Position', [100, 100, 1049, 695]);
% FigHandle = figure (3);
%   set(FigHandle, 'Position', [100, 100, 1049, 695]);
%% Allocating Space
nummax = 20000;
mckeffp = zeros(1,nummax-1);
```

```
thermp = zeros(1,nummax-1);

mcr_o = thermp;

mcl_E = thermp;

mcl_A = thermp;

mcl_C = thermp;

mct_wick = thermp;

mct_wall = thermp;

error = thermp;

dT = thermp;

Qt = thermp;

%% Materials

% Copper

rhoCu= 8960;                % kg/m^3        [density of copper]

kCu  = 397;                 % W/mK          [conductivity of Cu]

% most densities

%from http://www.engineeringtoolbox.com/density-solids-d_1265.html

% most thermal k

%from http://www.engineeringtoolbox.com/thermal-conductivity-d_429.html

%       some also from

%https://www.electronics-cooling.com/2001/05/the-

%thermal-conductivity-of-unfilled-plastics/

% most costs/kg
```

```
%from http://plasticker.de/preise/pms_en.php?show=
% ok&make=ok&aog=A&kat=Mahlgut
%       some also from
%http://web.mit.edu/course/3/3.11/www/modules/props.pdf
% ORDER:
%Copper   PP      ABS     Nylon66 HDPE    PVC     Rubber
%PMMA    PET     Glass   Iron    Nickel  SS      Al
rhoAD   = [8960 900 721 1150 1000 833 801 1190 1380 2600 7870 8900...
7700 2700];
kAD     = [397 0.2 0.18 0.25 0.48 0.19 0.10 0.21 0.2 1.05 80 91 16 205];
cAD     = [5.46 0.60 0.72 0.62 0.61 0.45 1.59 3.00 0.37 1.35 0.20 6.10...
2.70 1.80];


% Water
kl   = 0.65;                % W/mK          [conductivity of H2O
uH2Ol= 1.00e-3;             % Pa*s          [viscosity of liquid H2O] *
uH2Ov= 1.23e-5;             % Pa*s          [viscosity of vapor H2O] *
%% Constant Properties
kl   = 0.60;                % W/mK          [conductivity of H2O
kCu  = 400;                 % W/mK          [conductivity of Cu]
K    = 5.68e-12;            % m^2           [wick permeability, from Hwang]
hfg  = 2257e3;              % J/kg          [initial latent heat of H2O]
```

```
kB   = 1.38e-23;            % m^2kg/s^2/K   [Boltzmann Constant]
M    = 18.02;               % g/mol         [molar mass of H2O]
R    = 8.314;               % J/K/mol       [Gas constant]
rng('shuffle')


for     adiabaticn    = 1:14
parfor number = 1:nummax


    dPc = 1;
    dPt = 0;
    dPv = 0;
    dTv = 0;
    Ra  = 0;
    uratio = 0;
    r_o           = 0.005+rand*0.005;         % 0.005     to  0.010    m
    l_E           = 0.05+rand*0.45;           % 0.050     to  0.500    m
    l_A           = 0.01+rand*0.49;           % 0.010     to  0.500    m
    l_C           = 0.01+rand*0.49;           % 0.010     to  0.500    m
    twick         = 0.0001;                   % constant              m
    twall         = 0.001;                    % constant              m
    r_n     = r_o-twall;            % m             [wick outer radius]
    r_i     = r_n-twick;            % m             [wick inner radius]
```

```
    Q       = 10;
    heatflux = 1;

T       = ones(1,8);
Twn     = ones(1,5);
while dPc > dPt && uratio < 0.3 && heatflux < 1000 && Q < 3000
Q = heatflux*2*pi*r_o*l_E*10000;
% heatflux = Q/2/pi/r_o/l_E/10000;
Qin     = Q;
s = 1;
t = 1;



%% Comparison
%% Changing Adiabatic material
kAd     = kAD(adiabaticn);
rhoAd   = rhoAD(adiabaticn);
cAd     = cAD(adiabaticn);
w = 1000;
%% Inputs
```

```
Tc   = 348;                % K             [condenser wall temperature]

e    = 0.50;               % void fraction [Volume fluid/Volume wick]

N    = 23;

% wss  = 0.20;               % spheres*      [ws*; N = 24]

wg   = 1.1e-3;             % m             [width of channels]

wss  = 1-N*wg/2/pi/r_n;    % spheres*      [ws*; N = variable]

ws   = wss*wg/(1 - wss);   % m             [fin thickness]

                           % number of channels


%% Initial calculations

l_eff= l_A + (l_E + l_C)/2; % m             [effective length]

ee      = 2*r_i/(2*r_i + ws);

kwickr   = kCu*(1-ee*(1-kl/kCu));

                           % W/mK          [conductivity of wick at condenser]

RwallE  = log(r_o/r_n)/(2*pi*l_E*kCu);

                           % K/W           [Evaporator wall resistance]

RwallC  = log(r_o/r_n)/(2*pi*l_C*kCu);

                           % K/W           [Condenser wall resistance]

RwickE  = (1-pi/4)/(2*kl*l_E*N);

                           % K/W           [Evaporator wick resistance]

RwickC  = log(r_n/r_i)/(2*pi*l_C*kwickr);

                           % K/W           [Condenser wick resistance]
```

```
kwicka  = kwickr;
Rwicka  = @(l) l/((r_n^2 - r_i^2)*pi*kwicka);
Rwalla  = @(l) l/((r_o^2 - r_n^2)*pi*kAd);
mdot    = Q/hfg;            % kg/s          [mass flow rate]
qdot    = Q/(l_E*2*pi*r_o); % W/m^2         [heat flux]
%% Temperature and Pressure Calculations
T(1)    = Tc;                              % set point
T(2)    = Q*(RwallC + RwickC) + T(1);      % liquid/vapor interface temperature
    T2C = T(2) - 273;                      % T(2) in Celcius
Pl(1)   = [0.61121*exp((18.678 - T2C/234.5)*(T2C/(257.14 + T2C)))]*10^3;
                                           % condenser saturation
                                           % % pressure, Buck
                                           % equation (Pa)
Pv(1)   = Pl(1) - qdot/(hfg*sqrt(M/(2*pi*kB*T(2))));
                                           % PVC
    vg      = XSteam('vL_T',T2C);
    a       = 0.5;
    hiC     = 2*a/(2-a)*1/sqrt(2*pi*R*T2C)*(((XSteam('hV_T',T2C))...
-XSteam('hL_T',T2C)))*10^3)^2/vg/T2C;
    RiC     = 1/hiC/(2*r_i*pi*l_C);    % Interface resistance
T(3)    = T(2) + Q*RiC;                % TVC
    T3C = T(3) - 273;
```

```
dPv(1)  = -4/pi^2*(mdot^2/(8*XSteam('rhoV_T',T3C)*r_i^4));
                                        % delta Pv over condenser
dTv(1)  = R*T(3)^2/(((XSteam('hV_T',T3C))-(XSteam('hL_T',T3C)))*10^3*Pv(1));
                                        % delta Tv over condenser
T(4)    = T(3) + dTv(1);                % Tv at condenser/adiabatic
    T4C = T(4) - 273;
Pv(2)   = Pv(1) + dPv(1);               % Pv at condenser/adiabatic
dPv(2)  = 8*uH2Ov*mdot*l_A/(XSteam('rhoV_T',T4C)*pi*r_i^4);
                                        % delta Pv over adiabatic
dTv(2)  = R*(T(4))^2/(((XSteam('hV_T',T4C))-(XSteam('hL_T',T4C)))*10^3*Pv(2));
                                        % delta Tv over adiabatic
T(5)    = T(4) + dTv(2);                % Tv at adiabatic/evaporator
    T5C = T(5) - 273;
Pv(3)   = Pv(2) + dPv(2);               % Pv at adiabatic/evaporator
dPv(3)  = mdot^2/(8*XSteam('rhoV_T',T5C)*r_i^4);
                                        % delta Pv over evaporator
dTv(3)  = R*T(5)^2/(((XSteam('hV_T',T5C))-(XSteam('hL_T',T5C)))*10^3*Pv(3));
                                        % delta Tv over evaporator
T(6)    = T(5) + dTv(3);                % Tv at evaporator
    T6C = T(6) - 273;
Pv(4)   = Pv(3) + dPv(3);               % Pv at evaporator
                                        % delta Pl over length of heat pipe
```

```
    vg      = XSteam('vV_T',T6C);
    a       = 0.5;
    hiE     = 2*a/(2-a)*1/sqrt(2*pi*R*T6C)*(((XSteam('hV_T',T6C))...
    -XSteam('hL_T',T6C)))*10^3)^2/vg/T6C;
    RiE     = 1/hiE/(2*r_i*pi*l_E);     % Interface resistance
T(7)    = T(6) - Q*RiE;                 % liquid/vapor interface temperature
T(8)    = Q*(RwallE + RwickE) + T(7);   % evaporator wall temperature
dPl     = 8*uH2Ol*(l_E+l_A+l_C)*mdot...
/((XSteam('rhoL_T',((T(7)+T(2))/2-273))*N*pi*(r_i)^4));
Pl(2)   = Pl(1) - dPl;                  % Pl at evaporator
Ra(1)   = ((1/Rwicka(l_C)) + (1/Rwalla(l_C)))^-1;
Ra(2)   = ((1/Rwicka(l_A/2)) + (1/Rwalla(l_A/2)))^-1;
Ra(3)   = Ra(2);
Ra(4)   = ((1/Rwicka(l_E*2)) + (1/Rwalla(l_E*2)))^-1;
Rhp     = (T(7) - T(2))/(Q);
Qa      = Qin*(1/sum(Ra) + 1/Rhp)^-1/sum(Ra);
% Qb      = (Rhp)/(sum(Ra) + Rhp)*Q;
%% Wall temperature profile
Tw      = Twn;
Twn(5)  = T(8);
Twn(1)  = T(1);
i = 2;
```

```
while i < length(Twn)
    Twn(i) = Twn(i-1) + Ra(i-1)*Qa;
    i = i + 1;
end
Twdiff  = Twn - Tw;
T           = fliplr(T);                % sets the evaporator at x = 0
Pv          = fliplr(Pv);
Pl          = fliplr(Pl);
Pvxdistr    = [0 l_E l_E+l_A l_E+l_A+l_C];
Tvxdistr    = Pvxdistr;
Tvplot      = [T(3) T(4) T(5) T(6)];
Pvplot      = Pv;

keff        = Q/(T(1) - T(8))*(l_E+l_A+l_C);
    massa   = (l_A)*pi*(r_o^2-r_i^2)*rhoAd;
    masse   = (l_E)*pi*(r_o^2-r_i^2)*rhoCu;
    massc   = (l_C)*pi*(r_o^2-r_i^2)*rhoCu;
    masst   = massa+masse+massc;
    keffp   = keff/masst;
Tdrop       = T(1) - T(8);

%% Sensitivity
```

```
%% Limits check

% Check sonic limit

u           = Q/(pi*r_i^2)/XSteam('rhoV_T',mean(Tvplot)-273)/hfg;

                            % m/s       [vapor velocity]

Rev         = XSteam('rhoV_T',mean(Tvplot)-273)*u*2*r_i...

/XSteam('my_pT',mean(Pv)/100000,mean(Tvplot)-273);

                            % --        [vapor Reynolds number]

c           = XSteam('wV_T',mean(Tvplot)-273);

                            % m/s       [vapor speed of sound]

uratio      = u/c;          % ratio to determine if limit is hit

% % Check heat flux limit

% heatflux    = qdot*10^-4;


% Check pressure drop limit

dPc     = 2*78.2e-3/(wg/2);            % Capillary pressure limit of grooves

dPvt    = Pv(1) - Pv(4);                % Vapor pressure drop

dPt     = dPvt + dPl;                   % Total pressure drop

t = t+1;

if dPt > dPc || uratio > 0.3 || heatflux > 1000

    fprintf('\n\nfor r = %3.4f, limit hit: ',r_o)

    if dPt > dPc

        fprintf('1. pressure\n')
```

```
        fprintf('dPt = %3.5f\ndPc = %3.5f\n',dPt,dPc)
        error(number) = 1;
    elseif uratio > 0.3
        fprintf('2. sonic\n u/c = %3.5f',uratio)
        error(number) = 2;
    elseif heatflux > 1000
        fprintf('3. heat flux\n q" = %3.5f',heatflux)
        error(number) = 3;
    elseif (T(1) - T(8)) < 0
        error(number) = 4;
    elseif Q<0
        error(number) = 5;
    elseif keffp<0
        error(number) = 6;
    else
    end
else
end
% Q = Q + 10;
heatflux = heatflux + 0.1;
end
dT(number)          = (T(1) - T(8));
```

```
Qt(number)          = Q;

mcmass(number)      = masst;

mckeffp(number)     = 1/keffp;

mccostp(number)     = cAD(adiabaticn)*massa;

thermp(number)      = masst/Q;

mcl_E(number)       = l_E;

mcl_A(number)       = l_A;

mcl_C(number)       = l_C;

mcr_o(number)       = r_o;

mct_wick(number)    = twick;

mct_wall(number)    = twall;

mcheatflux(number)  = heatflux;

number

end

saverfile=sprintf('mcvariables%d',adiabaticn)

save(saverfile,'thermp','mckeffp','mccostp','mcmass','dT','Qt')


% f2 = figure (2);

% plotting_fronts(adiabaticn)


f1 = figure (1);

hold on
```

```
plot(mccostp,thermp,'.','Color',colors(adiabaticn))

xlabel('cost / Heat dissipated ($ / W)')

ylabel('thermal performance (kg / W)')

title({'50,000 calculations','','Lengths, materials, & r_o changed'})

drawnow


end

j=find(thermp==min(thermp));

i=find(mckeffp==min(mckeffp));

opt_parameters_calc(j,i,mcl_E,...

mcl_A,mcl_C,mcr_o,mct_wick,mct_wall,mckeffp,thermp);


% saveas(f1,'montecarlo_r_Le_La_Lc_10k_mdQ.png')

delete(gcp('nocreate'))
```